

# Accurate determination of chemical abundances near a supermassive black hole

Received: 24 July 2025

Accepted: 19 February 2026

Published online: 31 March 2026

 Check for updates

The XRISM Collaboration\*

The metal abundances in galactic nuclei carry key information on the history of star formation and mass transfer in central regions of galaxies. X-ray fluorescence analysis is a unique tool to reliably measure the abundances of various elements via simple physics. Here we present a new observation of the active nucleus in the Circinus galaxy with the XRISM satellite at unprecedented X-ray energy resolution. The fluorescent iron  $K\alpha$  line profile modified by Compton scattering indicates that the material responsible for its emission is cold and metal rich and is located  $\gtrsim 0.024$  pc from the supermassive black hole, consistent with the dusty torus region. The abundance pattern derived from comparing fluorescent line intensities of different metals shows subsolar ratios of argon- and calcium-to-iron and a supersolar ratio of nickel-to-iron. This abundance pattern is best produced by a combination in number fraction of  $92^{+2}_{-4}\%$  core-collapse supernovae from progenitor stars less massive than  $20^{+3}_{-2} M_{\odot}$  and  $8^{+4}_{-2}\%$  type Ia supernovae. This suggests that gas feeding the supermassive black hole was enriched by recent core-collapse supernovae. Our findings imply that in metal-rich environments stars more massive than about  $20 M_{\odot}$  directly collapse into black holes or make faint supernovae without ejecting heavy metals into the space.

The elemental abundance pattern is a crucial indicator for comprehending the history of metal production and supply in metal-enriched systems<sup>1</sup>. It reflects the history of past supernovae (SNe) of various types, roughly divided into type Ia SNe (SNe Ia) and core-collapse SNe (CCSNe). Metals produced by SNe are eventually supplied to intra-cluster medium and pollute its primordial gas synthesized by the Big Bang, consisting mainly of hydrogen and helium. X-ray observations of hot intracluster medium in galaxy clusters (for example, ref. 2) suggest that the metal abundance ratios integrated over the cosmic time are close to the solar values, which refer to the protosolar table of Lodders et al.<sup>3</sup> in all X-ray spectral models employed in this work. This abundance pattern can be explained by a combination of about 20% of SN Ia and about 80% of CCSN events according to current SN nucleosynthesis models<sup>4,5</sup>. However, probing the chemical abundance in the very central region of a galaxy, which holds a key to deciphering

its evolutionary history, has remained challenging. In the ultraviolet, optical and near-infrared bands, metal abundances in galaxies hosting supermassive black holes (SMBHs) are measured with emission-line ratios from nebulae via photoionization modelling, which traces primarily the interaction of optical and ultraviolet photons with the surrounding gas (for example, refs. 6–8). However, the results sensitively depend on the assumed density distribution, the shape of the ionizing continuum and the degree of dust depletion<sup>6,7</sup>, leaving large systematic uncertainties. By contrast, the interaction between X-rays and matter is simpler, permitting a nearly unbiased probe of all matter including gas and dust. A fluorescence line is emitted after photoelectric absorption of a high energy photon by an atom, and hence, its intensity represents the amount of each metal contained in X-ray irradiated medium. Thus, diagnostics based on fluorescence lines in the X-ray spectrum reflected off matter surrounding the SMBH enable a more direct estimate of the

\*A list of authors and their affiliations appears at the end of the paper. ✉ e-mail: [fukushima.kotaro@jaxa.jp](mailto:fukushima.kotaro@jaxa.jp); [sogawa@ac.jaxa.jp](mailto:sogawa@ac.jaxa.jp); [ueda@kusastro.kyoto-u.ac.jp](mailto:ueda@kusastro.kyoto-u.ac.jp); [uematsu@kusastro.kyoto-u.ac.jp](mailto:uematsu@kusastro.kyoto-u.ac.jp)

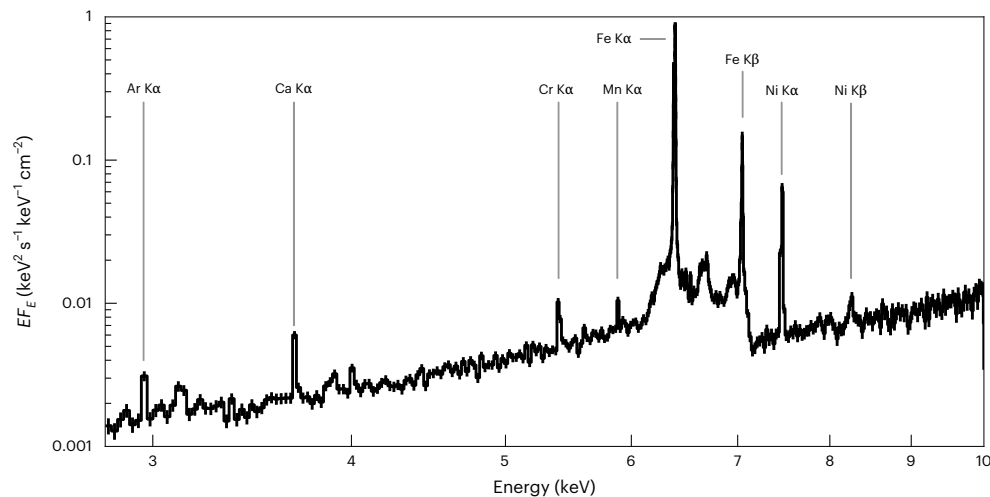


**Fig. 1 | XRISM/Resolve spectrum of the Circinus galaxy in the 2.8–10-keV band.** It is folded by the instrumental response in units of  $EF_E$ , where  $F_E$  is the energy flux at energy  $E$  (that is, corrected for the effective area). The spectrum is binned according to the ‘optimal binning’ technique<sup>82</sup>, which is used for the

spectral analysis throughout the Article. The non-X-ray background component is subtracted. Major fluorescence lines from cold matter are labelled. The error bars denote the  $1\sigma$  confidence limits in photon statistics.

elemental abundances in the environments of active galactic nuclei (AGNs). Thanks to its unprecedented energy resolution, the Resolve spectrometer onboard the recently launched X-ray observatory XRISM<sup>9</sup> enables the precise measurement of faint fluorescence emission lines from elements that were previously beyond reach.

In this study, we focus on the Circinus galaxy (hereafter Circinus), a nearby (4.2 Mpc; ref. 10), spiral galaxy hosting the nearest Seyfert 2 nucleus<sup>11</sup>. Previous X-ray observations have revealed that Circinus harbours a Compton-thick AGN (for example, refs. 12–14), where the central engine is heavily obscured by intervening material with a hydrogen column density of  $N_{\text{H}} > 10^{24} \text{ cm}^{-2}$ . This makes it an ideal target for studying the properties of the obscuring torus and its reflection spectrum.

Circinus was observed by XRISM on 8–12 February 2024, with a total exposure time of 309 ks. Nearly simultaneous NuSTAR and XMM-Newton observations were carried out to extend our spectral coverage to higher energies and to obtain better spatial resolution below 10 keV. The overall XRISM/Resolve spectrum covering an approximately  $3' \times 3'$  area centred at the Circinus nucleus is plotted in Fig. 1, where a wealth of emission lines from various elements are noticeable. Its enlarged view around the fluorescence lines of argon, calcium, chromium, manganese, iron and nickel is shown in Fig. 2a–g.

Our primary goal is to model the reflection spectrum from the AGN torus<sup>15</sup>, most probably located at about 0.1–10 pc from the SMBH<sup>16</sup> in Circinus, with a particular focus on the fluorescence lines from cold matter. To this end, we employed an updated version of the state-of-art clumpy torus model, XCLUMPY<sup>14</sup>, which accounts for the non-uniform distribution of matter in the AGN environment (‘Spectral model description’ section in the Methods). To accurately model the fluorescent line shapes, we incorporated the natural line widths determined from laboratory measurements. This approach is crucial for taking full advantage of the high-spectral resolution provided by XRISM/Resolve. Considering the limited photon statistics below  $\sim 2.5$  keV in the Resolve spectrum (Extended Data Fig. 1), here, we focus on the lines from Ar and heavier elements. Accordingly, the abundances of Ar, Ca, Cr, Mn, Fe and Ni were left as free parameters.

We simultaneously fitted the XRISM/Resolve spectrum in the 2.0–10-keV band and the NuSTAR one in the 8–70-keV band. The model consists of the torus reflection component described above, transmitted component, emission from ionized gas and emission from contaminating sources other than the AGN (‘Analysis of contaminating sources’ section in the Methods). To take into account Doppler broadening of

lines, we convolve the line components from the torus with a Gaussian kernel. This model is found to well reproduce the whole spectra.

We have obtained the best quality spectrum of a narrow iron K $\alpha$  line (Fig. 3) ever observed from an AGN (see Extended Data Fig. 2 for a comparison with the Chandra/HETG data). It is characterized by its narrowness, with full width half maximum (FWHM) of  $210 \pm 10 \text{ km s}^{-1}$ , which was overestimated in previous studies (for example, refs. 17,18), most probably due to the non-consideration of the fine structure and/or natural broadening in the intrinsic line profile<sup>19</sup> and to spatial-spectral degeneracies in grating data<sup>20</sup>. The width is larger than those of atomic and molecular lines at 0.5–4 pc ( $115.2 \pm 0.8 \text{ km s}^{-1}$  in FWHM for  $[\text{C I}]^3\text{P}_1\text{--}^3\text{P}_0$  and  $141.1 \pm 0.8 \text{ km s}^{-1}$  in FWHM for  $\text{CO}(J=3 \rightarrow 2)$ , where  $J$  is the total angular momentum quantum number) but is smaller than that of ionized gas in the central core ( $< 0.5$  pc), traced by the atomic hydrogen recombination line, H36 $\alpha$ , at 135 GHz with ALMA ( $393 \pm 44 \text{ km s}^{-1}$  in FWHM)<sup>21,22</sup>. To infer the innermost radius of the line emitter, we convolve the intrinsic line profile with a kernel that represents Doppler broadening by a Keplerian disk (`rdblur` in XSPEC) instead of a Gaussian. Adopting an inclination of  $79.1^\circ$ , the best-fit value in the XCLUMPY spectral fitting (Extended Data Table 1), and assuming an outermost radius of  $10^8 r_g$  ( $r_g \equiv GM/c^2$  is the gravitational radius, where  $G$ ,  $M$  and  $c$  are the gravitational constant, black hole (BH) mass and light velocity, respectively), which roughly corresponds to the size of the nuclear dust continuum emission imaged by ALMA<sup>21</sup>, we obtain an emissivity index of  $q = -1.7 \pm 0.1$  and an innermost radius of  $(3.0 \pm 0.6) \times 10^5 r_g$ , which corresponds to  $0.024 \pm 0.007$  pc for an SMBH mass of  $(1.7 \pm 0.3) \times 10^6 M_\odot$  (ref. 23). This is almost consistent with the dust sublimation radius of the torus in Circinus,  $0.05 \pm 0.02$  pc (ref. 20), assuming a factor of 2 uncertainty in the bolometric luminosity. Another key feature is the smeared shape of the low energy side of the Compton shoulder structure (refs. 24,25) at 6.24 keV (corresponding to the backscattering case by a free electron at rest). When X-rays are scattered by electrons bound in atoms, the edge feature is blurred by an order of the electron binding energies due to the Doppler broadening. Hence, our result suggests that the scatterer is likely to be cold (not-ionized) material. Within our measurement uncertainties, the centroid energy of the Fe K $\alpha$  line is consistent with the rest-frame energy of cold atom (‘Spectral model description’ section in the Methods), indicating that the bulk of the reflecting material is not undergoing significant systematic motion relative to the host galaxy, unlike the optical lines from the ionization cone that show blueshifts of  $\geq 200 \text{ km s}^{-1}$  (refs. 26,27). All these considerations suggest that the Fe K lines predominantly come from an innermost part of the ‘cold’, dusty

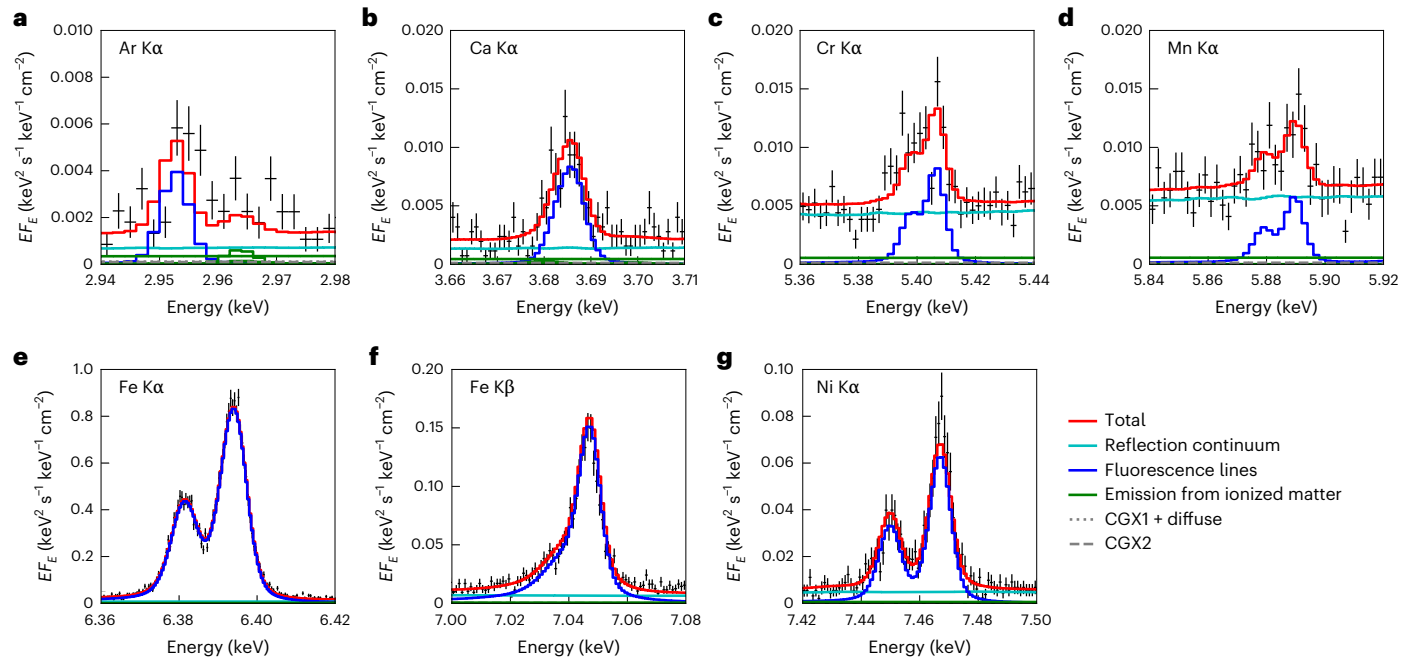


**Fig. 2 | Enlarged plots of the XRISM/Resolve spectrum of the Circinus galaxy around the major fluorescence lines from neutral matter, overlaid with the best-fit model. a–g, Ar K $\alpha$  (a), Ca K $\alpha$  (b), Cr K $\alpha$  (c), Mn K $\alpha$  (d), Fe K $\alpha$  (e), Fe K $\beta$  (f) and Ni K $\alpha$  (g). They are folded by the instrumental response in units of  $EF_E$ , where  $F_E$  is the energy flux at energy  $E$ . The observed data are plotted in black with error bars denoting the  $1\sigma$  confidence limits in photon statistics. The blue,**

cyan, green and red lines represent the emission lines from cold matter, the reflection continuum from cold matter, emission from ionized matter together with the Thomson-scattered component and the total, respectively, based on our best-fitting model ('Spectral model description' section in the Methods). For visualization, the bin size is set at either 2 eV (Ar K $\alpha$ , Cr K $\alpha$  and Mn K $\alpha$ ), 1 eV (Ca K $\alpha$ , Fe K $\beta$  and Ni K $\alpha$ ) or 0.5 eV (Fe K $\alpha$ ) in these plots.

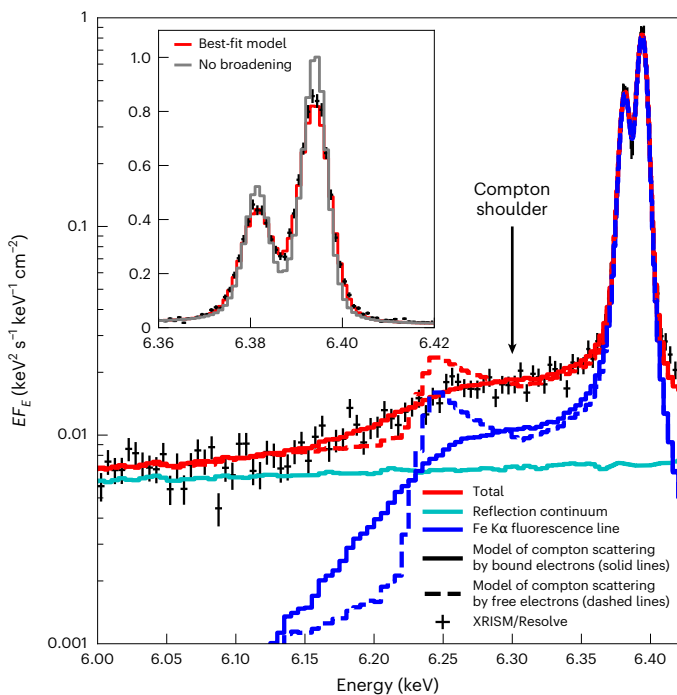


**Fig. 3 | A zoom-in picture of XRISM/Resolve spectrum of the Circinus galaxy around the Fe K $\alpha$  emission line. They are folded by the instrumental response in units of  $EF_E$ , where  $F_E$  is the energy flux at energy  $E$ . The observed data are plotted in black with error bars denoting the  $1\sigma$  confidence limits in photon statistics. The blue, cyan and red lines represent the models of the emission lines from cold matter, the reflection continuum from cold matter and the total, respectively. The dashed lines denote the case where Compton scattering from free electrons at zero temperature is considered. In the inset, the observational data are compared against our best-fit model (red) and a model to which no Gaussian broadening is applied (grey). This shows that Doppler broadening is very small compared with the intrinsic width of the Fe K $\alpha$  line.**

torus, which dominates the mass distribution of the surrounding matter. We note, however, that although our Circinus spectrum does not require contributions from the broad line region as discussed by Gandhi et al.<sup>28</sup> and Andonie et al.<sup>18</sup>, it may be due to the heavy obscuration by the torus that completely blocks emission inside it. In fact, XRISM observations of less obscured AGNs commonly show broader components in Fe K $\alpha$  (for example, ref. 29).

We have accurately determined the abundance ratio of iron to hydrogen is  $2.3 \pm 0.1$  times the solar value through a joint analysis of the broadband spectra and iron K $\alpha$  profile (see 'Spectral model description' section in the Methods for details). The shape of the broadband reflection continuum basically determines the geometry and hydrogen column density of the torus. Then, as in previous studies<sup>30</sup>, the equivalent width of iron K $\alpha$  can be used to infer the Fe/H abundance ratio. To obtain a tighter constraint on Fe/H, we additionally utilize the intensity of iron K $\alpha$  and its Compton-shoulder fraction  $f_{CS}$ , which are roughly proportional to the amount of iron atoms and hydrogen atoms in the reflector, respectively<sup>24</sup>. We have confirmed that our results on the Fe/H abundance ratio is robust against different parameters of the torus geometry ('Effects by adopting different torus geometry' section in the Methods).

Figure 4 shows the observed abundance ratios relative to iron in the Circinus centre. The Ar/Fe and Ca/Fe ratios exhibit subsolar (0.6–0.8) values, whereas the Ni/Fe ratio is supersolar (1.3). Our abundance pattern differs from that of the Perseus cluster core<sup>2,31</sup>, which follows the solar abundance ratios including Ni/Fe, and from nuclear star clusters in the Milky Way<sup>32</sup>, which show subsolar Ca/Fe but supersolar Mn/Fe ratios.

To interpret our result, the observed abundance pattern is modelled by using a linear combination of CCSN and SN Ia nucleosynthesis predictions (for example, ref. 31), yielding the abundance ratio of element X to iron as

$$\frac{A_X}{A_{Fe}} = \frac{r^{Ia} A_X^{Ia} + A_X^{CC}}{r^{Ia} A_{Fe}^{Ia} + A_{Fe}^{CC}},$$

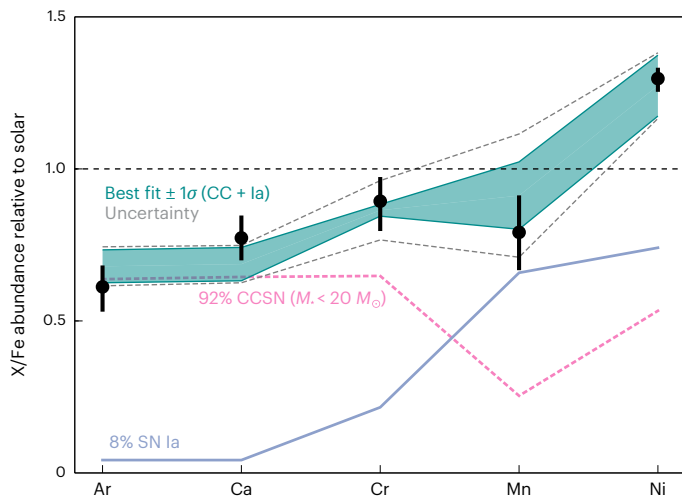


**Fig. 4 | Observed elemental abundances of the Circinus centre and theoretically calculated values with an upper mass limit of  $20 M_{\odot}$  for CCSN progenitors.** Relative abundances with respect to iron determined with XRISM (X/Fe, filled circles) normalized to the corresponding protosolar values (horizontal dashed line). The error bars denote the  $1\sigma$  confidence limits on the measurement, estimated by Markov chain Monte Carlo method. The green shaded area represents the  $1\sigma$  statistical uncertainty region of the best-fit model ( $\sigma_{\text{stat}}$ ) consisting of 92% CCSNe from progenitor stars with zero-age main-sequence masses ( $M$ ) smaller than  $20 M_{\odot}$  and 8% near- $M_{\text{Ch}}$  SNe Ia in number fraction. The contribution that CCSNe and SNe Ia make to the X/Fe are represented by the magenta and blue curves, respectively. Here, we adopt the nucleosynthesis models for CCSNe<sup>4</sup> and SNe Ia<sup>5,35</sup>. The thin, dashed grey lines show the total uncertainty, including differences in the predicted yields by alternative SN Ia and CCSN modelling as  $\sqrt{\sigma_{\text{stat}}^2 + \sigma_{\text{Ia}}^2 + \sigma_{\text{CC}}^2}$  (‘Metal enrichment models’ section in the Methods).

where  $f^{\text{a}}$  denotes the number ratio of SNe Ia to CCSNe. Progenitors for each SN type are assumed to have the solar metallicity ( $Z = 0.02$ ). The Salpeter initial-mass function (IMF, index of  $-2.35$ ; ref. 33) is employed to integrate yields over CCSNe progenitor masses ranging from  $9 M_{\odot}$  to  $M_{\text{CCSN,up}}$

$$A_{\text{X}}^{\text{CC}} = \frac{\int_{9M_{\odot}}^{M_{\text{CCSN,up}}} M^{-2.35} A_{\text{X}}(M) dM}{\int_{9M_{\odot}}^{M_{\text{CCSN,up}}} M^{-2.35} dM},$$

where  $A_{\text{X}}(M)$  represents the yield of element X as a function of the progenitor mass  $M$ . When  $A_{\text{X}}(M)$  is available only at discrete values of  $M$  in the literature, we simply refer to the value closest to each calculation point in the integration. Here, we assume that all stars formed according to the IMF in the integrated mass range have already undergone CCSNe. This assumption is valid because the young nuclear stellar population in Circinus has estimated ages of  $4 \times 10^7 - 1.5 \times 10^8$  yr (ref. 34), which is comparable or longer than the life time of a star with an initial mass of  $9 M_{\odot}$ . For the metal yields, we refer to the well-established CCSN model by Nomoto et al.<sup>4</sup>, alongside with the SN Ia yields from near-Chandrasekhar-mass ( $M_{\text{Ch}}$ ) progenitors<sup>5</sup> and merging sub- $M_{\text{Ch}}$  ones<sup>35</sup>. Note that CCSNe from high mass ( $\geq 20 M_{\odot}$ ) progenitors produce a large amount of  $\alpha$  elements relative to iron, compared with SNe Ia<sup>4,5</sup>.

Although detailed studies on the origin of the metals in Milky Way stars (for example, ref. 36) consider star formation history to explain the evolution of chemical elements over the cosmic time, in this study, we focus on the relative contributions from different explosion sites (for example, the initial-mass-dependent SN yields), which determine the abundance ratios among the heavy elements. We do not assume that the SNe Ia and CCSNe originate from the same stellar population or consider star formation histories representing the detailed metal

enrichment history. The delay time distribution of SNe Ia after birth typically ranges from 100 to 1,000 Myr (for example, ref. 37), whereas that of CCSNe is much shorter ( $< 50$  Myr for a single massive progenitor<sup>38</sup>). Thus, the fraction of CCSNe estimated by our analysis provides key information on contribution from young star formation at the central region of Circinus. Throughout the paper, we assume that the AGN does not influence stellar evolution and distribution of elements.

As a reference model, we first consider a wide mass range for CCSN progenitors by setting  $M_{\text{CCSN,up}} = 40 M_{\odot}$  with contribution of near- and sub- $M_{\text{Ch}}$  SNe Ia. The five abundance ratios (Ar/Fe, Ca/Fe, Cr/Fe, Mn/Fe and Ni/Fe) are compared with model predictions by varying the number fractions of three SN types (that is, with two independent free parameters). The fitting is performed by minimizing the  $\chi^2$  statistics. We find that the observed pattern can be roughly explained by a combination of 60% CCSNe and 40% SNe Ia in number fraction (Table 1 and Extended Data Fig. 3). However, the fitting is not statistically acceptable with reduced  $\chi^2$  of 3.3. Furthermore, the typical SN Ia fraction even in ancient systems, such as galaxy clusters and early-type galaxies, varies from 10% to 25% (for example, see ref. 31 for a recent comprehensive study); therefore, the substantial SN Ia contribution higher than this level is hard to interpret for the Circinus centre, wherein a continuous star formation is identified<sup>39,40</sup>. Thus, this reference model is not favoured due to both statistical and physical issues.

Alternatively, we select a different mass range for CCSN progenitors by employing IMF-weighted integrations with the upper mass limits in the range of  $M_{\text{CCSN,up}} = 18 - 35 M_{\odot}$ . As summarized in Table 1, the models with  $M_{\text{CCSN,up}} < 30 M_{\odot}$  give statistically much better fits to the observed abundance pattern than the SNe Ia dominant model, and produce a natural enrichment scenario, with a dominant contribution from CCSNe. Figure 4 shows the best-fitting combination model, where the number fraction of CCSNe with progenitors less massive than  $20_{-2}^{+3} M_{\odot}$  is  $92_{-4}^{+2}\%$ , globally reproduces the abundance ratios of Ar, Ca, Cr, Mg and Ni, relative to Fe. The attached errors are statistical ones at  $1\sigma$  confidence limits; we estimate that in  $M_{\text{CCSN,up}}$  from the  $M_{\text{CCSN,up}}$  versus  $\chi^2$  plot with  $1 M_{\odot}$  steps. The ‘Metal enrichment models’ section in the Methods summarizes other modelling trials assuming different SN Ia models or CCSNe models with alternative yield calculation, IMF, hypernova (HN) contribution and progenitor metallicity. We confirm that our conclusions are not affected. The systematic uncertainty in

**Table 1 | The best-fitting number fraction of each type of SN to reproduce the observed abundance ratios of Ar/Fe, Ca/Fe, Cr/Fe, Mn/Fe and Ni/Fe in the Circinus centre**

$M_{\text{CCSN,up}}^{\text{a}}$	SN Ia (%)		CCSN (%)	Reduced $\chi^2$ (Degrees of freedom)
	Near- $M_{\text{Ch}}^{\text{b}}$	Sub- $M_{\text{Ch}}^{\text{c}}$		
$Z_{\text{CCSN}} = 0.02$ (solar metallicity)				
$40 M_{\odot}$	19	21	60	3.32 (3)
$35 M_{\odot}$	18	19	63	3.14 (3)
$30 M_{\odot}$	17	17	66	2.73 (3)
$25 M_{\odot}$	13	18	78	1.90 (3)
$20 M_{\odot}$	8	0	92	1.12 (3)
$18 M_{\odot}$	9	1	90	1.60 (3)
$Z_{\text{CCSN}} = 0.05$ (supersolar metallicity)				
$40 M_{\odot}$	14	22	64	2.90 (3)
$25 M_{\odot}$	8	9	73	1.47 (3)
$20 M_{\odot}$	5	3	92	1.06 (3)
$18 M_{\odot}$	5	2	93	1.16 (3)

Different assumptions on the upper mass limits for CCSN progenitors are adopted. <sup>a</sup>Upper mass limit for CCSN progenitors. <sup>b</sup>SN Ia from near- $M_{\text{Ch}}$  progenitors. <sup>c</sup>SN Ia from sub- $M_{\text{Ch}}$  progenitors.

the CCSN or SN Ia fraction is found to be 2%, which is smaller than the statistical one.

Our findings indicate two important consequences on SMBH-galaxy co-evolution and on the mechanisms of CCSNe. The SN composition suggests that the SMBH is accreting gas whose metal is largely enriched by recent CCSNe rather than old gas produced by SNe Ia. This does not contradict the ‘inside-out’ galaxy formation scenario, where the core of a galaxy formed in the very early universe<sup>41</sup>, if gas in the torus region <10–20 pc is continuously supplied from the outer disk, replacing old gas (‘Mass transfer in circinus centre’ section in the Methods). The co-existence of nuclear starburst and AGN activities is in line with models where SNe play a role for obscuration of the central engine<sup>42</sup>. Also, high metallicity in galactic nuclei implies the importance of AGN feedback as a metal enrichment process on galaxy scales and beyond<sup>43</sup>.

The presence of an upper mass limit for CCSN progenitors at the galactic central region has a critical implication for our understanding of the fate of massive stars. Our scenario is consistent with the suggestion by Mao et al.<sup>44</sup> based on the chemical abundance measurement of the hot atmosphere of a starburst galaxy. Some theories postulate that stars with zero-age main-sequence masses ( $M_{\text{ZAMS}}$ ) of a few tens of solar masses will not undergo CCSN explosions but directly collapse into BHs (for example, ref. 45) or make faint SNe without emitting heavy metals<sup>46</sup>. Observationally, although there are a few possible examples for such BH-forming events in the local universe<sup>47</sup>, it is still controversial whether this channel can make a substantial contribution to the BH population. Our finding supports the direct BH-forming collapses or faint SNe for stars with  $M_{\text{ZAMS}} > 20^{+3}_{-2} M_{\odot}$  in metal-rich environments unless massive stars are not formed due to, for example, a severely distorted IMF. This scenario may also solve the ‘red supergiant (RSG) problem’ (for example, refs. 48, 49) that no CCSNe from RSG stars with  $M_{\text{ZAMS}} > 18 M_{\odot}$  have been found in the local universe despite the existence of more massive RSGs. In addition, it gives an important clue to understand nucleosynthesis history in the universe. We infer that, in the early universe when the gas is metal poor, very massive stars (for example,  $M_{\text{ZAMS}}$  of several tens of solar masses beyond the BH-forming mass window) explode as CCSNe and produce a large amount of alpha elements, to explain the solar abundance ratios in galaxy clusters<sup>2,31</sup>.

## Methods

### XRISM data reduction

We used Heasoft version 6.34 and XRISM Calibration Database version 20240815 for the data reduction. The Resolve data were reduced according to the XRISM Quick Start Guide v2.3, and additional screening was applied using the standard energy-dependent rise time cut<sup>50</sup>. The response matrix file was generated using RSLMKRMF, and its normalization was calculated based on the event grade distribution in the cleaned event file. The cleaned file initially included low-resolution secondary events, which were not caused by the source but resulted from the secondary-pulse detection algorithm processing clipped pulses. As almost all events should have a high-resolution primary grade due to the count rate of  $10^{-3}$  to  $10^{-1} \text{ s}^{-1}$  per pixel, the low-resolution secondary events were removed from the cleaned event file before calculating the response matrix file. The ancillary response file was created with XAARFGEN, assuming a point-like source at the aim point as input. Only high-resolution primary grade events were used for spectral analysis.

The gain and thus the energy scale of Resolve is sensitive to its environment. Thus, the gain is monitored using onboard calibration sources during fixed fiducial intervals in the standard Resolve calibration strategy<sup>51</sup>. The fiducial intervals are then interpolated to reconstruct the time-dependent energy scale. The efficacy of this strategy is monitored by a continuously illuminated calibration pixel that is located just outside the aperture of the instrument, but part of the 50-mK detector array. The calibration pixel is continuously illuminated by a heavily collimated <sup>55</sup>Fe source but is corrected using the same

fiducial intervals as the main array. For this observation, the calibration pixel energy scale offset was measured to be 0.07 eV at 6 keV. This is added in quadrature to the systematic uncertainty in the Resolve energy scale, which is the standard method for Resolve observations. The systematic uncertainty in the Resolve energy scale is 0.3 eV from 5.4–9 keV (the range of the suite of onboard calibration sources)<sup>52</sup>. Added in quadrature, the systematic uncertainty in the energy scale for this observation is thus 0.31 eV. During the fiducial intervals, the energy resolution of the composite spectrum of the main array was 4.44 eV at 5.9 keV, which is in-line with the standard XRISM/Resolve RMF.

The XRISM/Resolve main array is composed of 36 pixels, one of which is the calibration pixel which is outside of the instrument aperture. For this observation, 34 main array pixels were used in the analysis. Pixel 27 was not used because it has been shown to exhibit gain jumps, which are not correctable with the sparse gain fiducials used in the standard energy scale reconstruction method.

The non-X-ray background (NXB) event file was generated using the RSLNXBGEN task, and it was screened with the same criteria as the source data, excluding pixel 27 and retaining only high-resolution primary grade events. The NXB spectrum was fitted using a model provided by the XRISM Calibration team, which includes a power-law component and 17 narrow emission lines modelled by Gaussian profiles. These lines correspond to Al K $\alpha$ 1/K $\alpha$ 2, Au M $\alpha$ 1, Cr K $\alpha$ 1/K $\alpha$ 2, Mn K $\alpha$ 1/K $\alpha$ 2, Fe K $\alpha$ 1/K $\alpha$ 2, Ni K $\alpha$ 1/K $\alpha$ 2, Cu K $\alpha$ 1/K $\alpha$ 2, Au L $\alpha$ 1/L $\alpha$ 2 and Au L $\beta$ 1/L $\beta$ 2. Extended Data Fig. 1 plots the observed spectrum of Circinus (not corrected for effective area) and this NXB model.

### NuSTAR observations and data reduction

The hard band spectrum of the Circinus galaxy was obtained with NuSTAR on 2 February 2024, with a total exposure time of 24 ks (ID 60901013002). We reprocessed the data from the two FPM detectors, following the standard procedure. The source spectrum was extracted from a circular region with a radius of 60 arcsec centred on the source peak. The background was taken from a circular region with a radius of 60 arcsec that is not contaminated by bright Chandra-detected sources or the PSF wings of the nucleus. The source spectra were binned to contain at least 50 counts per bin.

### Analysis of contaminating sources

The Resolve spectrum of the Circinus galaxy is mainly contaminated by three sources: CGX1 (ultraluminous X-ray source), CGX2 (supernova remnant), and diffuse emission (see refs. 13, 53–55). To constrain the impact of these contaminating sources, we utilized the high-spatial-resolution image obtained with XMM-Newton. The Circinus galaxy was observed with XMM-Newton from February 2 2024 to February 3 2024, with a total exposure time of 115 ks (ID 0932990101). The unfiltered data were reprocessed following the standard procedure with SAS V21.0.0. We extracted two types of spectra with the following recipe. First, the ‘XMM-all’ spectrum, which contains nearly all of the contaminating sources in the Resolve spectrum, was extracted from a circular region with a radius of 90 arcsec centred on the Circinus galaxy, thus commensurate to the Resolve field-of-view. Here, we utilized the pn data, which have better photon statistics than the MOS1 or MOS2 data. The background spectrum for the ‘XMM-all’ spectrum was extracted from a source-free annulus with an inner radius of 100 arcsec and an outer radius of 140 arcsec. Second, the ‘XMM-CGX2’ spectrum, which represents the source spectrum of CGX2, was extracted from a circular region with a radius of 8 arcsec centred on CGX2. For this we utilized the MOS1 data, which have the best spatial resolution among the three EPIC cameras. The background spectrum for the ‘XMM-CGX2’ spectrum was extracted from three circular regions, each with a radius of 8 arcsec and located at the same distance from the Circinus galaxy. The image of MOS1 is displayed in Supplementary Fig. 1, where the source and background regions for the ‘XMM-CGX2’ spectra are indicated, together with the corresponding source region for the ‘XMM-all’

spectrum. All the source spectra are binned to contain at least 50 counts per bin. Note that there is a known issue in the cross calibration between NuSTAR and XMM-Newton<sup>56</sup>. To correct this issue, we always applied the `applyabsfluxcorr=yes` option in ARFGEN.

To better constrain the CGX2 spectrum, we also utilized the high spatial and energy resolution spectra obtained with Chandra/HETG. The Circinus galaxy was observed with Chandra/HETG for several times from 8 December 2008 to 4 March 2009 (IDs 10223, 10224, 10225, 10226, 10832, 10833, 10842, 10843, 10844, 10850, 10872 and 10873). We reprocessed all the spectra following the standard procedure with CIAO V4.17. The combined spectra were binned to contain at least one count per bin.

First, we calibrated the spectral model for CGX2 utilizing the Chandra/HETG spectra. We simultaneously fitted the HEG (first order), the MEG (second order) and the zeroth order spectra with a constant temperature plane-parallel shock plasma model modified by Galactic absorption of  $N_{\text{H}} = 7.02 \times 10^{21} \text{ cm}^{-2}$  (ref. 57). The model is expressed as follows in XSPEC terminology:

$$\text{CGX2} = \text{TBabs} * \text{bvps shock}$$

We successfully reproduced the spectra ( $C$  statistic = 4,454.6 for 4,536 degrees of freedom) with this model, which gives a similar spectrum to that adopted by Arévalo et al.<sup>13</sup>. Note that the `TBabs` model implements the photoelectric absorption cross-section in the interstellar medium given by Wilms et al.<sup>58</sup> and assumes one solar abundances.

Supplementary Fig. 2 plots the Chandra/HETG spectra together with the best-fit model. Next, we fitted the ‘XMM-CGX2’ spectrum with the calibrated model described above. Here, we left the normalization to vary to treat the known time variability of CGX2<sup>59</sup>. We well reproduced the ‘XMM-CGX2’ spectra with  $\chi^2 = 21.1$  for 26 degrees of freedom. The combined spectrum of CGX1 and the diffuse emission was approximated by a single power-law with a cutoff at 10 keV, which was expressed as `zcutoffpl` in XSPEC terminology. Although Arévalo et al.<sup>13</sup> adopted a simple absorbed power-law model for CGX1, the difference little affects the spectral fitting of the nuclear emission, which is much harder than the CGX1 spectrum.

The model to fully characterise the contribution of the contaminating sources in the XRISM/Resolve and NuSTAR apertures was determined by fitting them together with the XMM-Newton/EPIC-pn spectra, by using models representing independently the AGN, CGX1 + diffuse and CGX2 contributions. The spectral model for the AGN component is described in the ‘Spectral model description’ section. The model and the parameters of CGX2 were fixed at the values as derived from the XMM-CGX2 spectra. We included a cross-normalization factor (relative to Resolve) to correct for a possible difference in the absolute flux calibration among different instruments. Note that the normalization of CGX2 was set to keep consistency with the cross-calibration factor.

### Spectral model description

As mentioned in ‘Main’, the reflection component from an AGN torus carry critical information on its geometry, hydrogen column density and metal abundances. Basically, the broad continuum is determined by the torus geometry and hydrogen column density<sup>14,60–63</sup>, whereas the equivalent width<sup>30</sup> and Compton shoulder fraction<sup>24</sup> of iron K $\alpha$  are determined by the Fe/H abundance ratio. It is noteworthy that the estimated torus parameters also depend on the intrinsic spectrum (photon index and high energy cutoff); for instance, a harder spectrum produces a stronger iron K $\alpha$  line because of a larger number of photoionizing photons above the iron K-edge energy. It is not easy to accurately determine the intrinsic spectrum in a heavily Compton-thick AGN, where the transmitted component is not directly observable. Thus, it is crucial to simultaneously fit the broadband continuum spectrum and high energy-resolution spectrum covering the iron K $\alpha$  band to best constrain the torus parameters by solving the degeneracy among them.

To derive the physical properties of the Circinus galaxy, we developed a new model that is applicable to the state-of-art high-resolution spectrum of XRISM. The basic idea of this model is based on the XCLUMPY model<sup>14</sup>, which was designed to reproduce the X-ray reflection from a clumpy torus based on the same formalism as in the CLUMPY model<sup>64</sup>. In XCLUMPY, spheres with a uniform density are distributed according to a Gaussian distribution (with a standard deviation of  $\sigma$ ) in the elevation direction and a power-law distribution with an index of  $-0.5$  in the radial direction. The inner and outer radii of the torus are set at  $r_{\text{in}} = 0.05$  pc and  $r_{\text{out}} = 1.0$  pc, respectively, and the radius of each clump is set at  $R_{\text{clump}} = 0.002$  pc. Note that XCLUMPY is a scale-free model (that is, the output spectra are identical as far as the ratios among these three parameters are kept the same). The expected value of number of blobs along the sight line on the equatorial plane is fixed at 10. The free parameters regarding the torus properties are the torus angular width ( $\sigma$ ), the total hydrogen column density in the equatorial plane ( $N_{\text{H}}^{\text{Equ}}$ ), and the inclination angle ( $i$ ). A cross-section view of the distribution of clumps in XCLUMPY is shown in Supplementary Fig. 3a. We expanded the parameter ranges to treat variable abundances and implemented the natural widths of prominent fluorescent lines referring to the following databases: Hölzer et al.<sup>19</sup> (Fe K $\alpha$ , Fe K $\beta$ , Co K $\alpha$ , Co K $\beta$ , Ni K $\alpha$ , Ni K $\beta$ , Cr K $\alpha$  and Cr K $\beta$ ), Hitomi Calibration report (Mn K $\alpha$  and Mn K $\beta$ ), Ito et al.<sup>65</sup> (Ca K $\alpha$  and Ca K $\beta$ ) and Krause and Oliver<sup>66</sup> (Ar K $\alpha$ ).

We fitted the Resolve and NuSTAR spectra with the updated version of XCLUMPY. The broadband Resolve-NuSTAR model is attributed to contributions from different components, as follows:

$$\text{const} \times (\text{AGN} + \text{CGX2} + \text{CGX1} + \text{diffuse}).$$

The first term (`const`) is a cross-normalization factor (relative to Resolve) to correct for a possible difference in the absolute flux calibration among different instruments. The model and the parameters of CGX2 and CGX1 + diffuse were fixed to the values found in the ‘Analysis of contaminating sources’ section. Their summed contributions in the XRISM/Resolve spectrum are approximately 1.1% at 5 keV and 0.2% at 10 keV.

In XSPEC terminology, the AGN component is expressed as follows:

$$\begin{aligned} \text{AGN} = & \text{TBabs} * \text{TBvarabs} * (\text{TBvarabs} * \text{cabs} * \text{zcutoffpl} \\ & + \text{xclumpy}_{\text{R.fits}} + \text{gsmooth} * \text{xclumpy}_{\text{L.fits}} \\ & + 3 * \text{pion} + \text{zcutoffpl}) \end{aligned}$$

The first term (`TBabs`) represents the Galactic absorption and the second one (`TBvarabs`) takes into account foreground absorption towards the nucleus in the host galaxy<sup>67,68</sup> with the same chemical abundances as in the XCLUMPY model. In the parenthesis, the first combination of terms describes the direct component transmitted through the torus. The second and third sets of terms represent the reflection continuum and the fluorescence lines from the torus. To detect energy shifts from the literature values<sup>19</sup>, the redshift parameters are allowed to vary. The line components are convolved with a Gaussian kernel to determine additional broadening. As discussed in ‘Main’, the bulk of the iron emitting material is constrained to a location at about 0.03 pc. Based on our analysis of the Chandra imaging data, spatially extended Fe K $\alpha$  line emission on a 100-pc scale, revealed by Marinucci et al.<sup>54</sup>, makes only a minor (<1%) contribution to the XRISM Fe K $\alpha$  signal. The metal abundances, photon index, cutoff energy and normalization are linked to those of the direct component. The last set of terms describe the emission from photoionized plasmas seen in the Resolve spectrum. The emission lines, radiative recombination continuum and bremsstrahlung emission produced by them are modelled with the `pioncode`<sup>69</sup>. In addition, we take into account the Thomson-scattered component (for example, ref. 70) of the direct emission (`zcutoffpl`),

which is not included in the  $\pi$ ion model, by setting its normalization to be consistent with the column density and covering fraction of the photoionized plasmas. Here, we ignore self-absorption by bound electrons. The detailed physical interpretation of this photoionized emission model will be discussed in a forthcoming study (Guainazzi et al., in preparation).

We simultaneously fitted the Resolve and NuSTAR spectra by adopting  $C$  statistics for the former and  $\chi^2$  statistics for the latter. Our model successfully reproduced the data: for a total of 30 free parameters, we obtain a  $C$  statistic = 2,695.8 for 2,316 bins (Resolve),  $\chi^2 = 213.4$  for 232 bins (FPMA) and  $\chi^2 = 216.4$  for 212 bins (FPMB). We confirm all AGN components introduced above are significantly required at >99% confidence limits. Supplementary Fig. 4 plots the spectra of Resolve and NuSTAR corrected for the effective area, the best-fit models for the total and the AGN component, and the fitting residuals. A zoom of Fig. 1, including only the energy range of the Fe K $\alpha$  and K $\beta$  fluorescent lines, is shown in Supplementary Fig. 5. The best-fit parameters of the AGN component, together with the parameters of the Gaussian kernel are summarized in Extended Data Table 1. The error on each parameter corresponds to a  $1\sigma$  confidence limit for a single parameter estimated by Markov Chain Monte Carlo method. Supplementary Fig. 6 presents the corner plot among the metal abundances. The high inclination angle we obtain,  $i = 79.1^\circ \pm 0.4^\circ$ , is compatible with estimates from other wavelengths:  $i > 70^\circ$  (ref. 71) and  $i > 83^\circ$  (ref. 72) from mid-infrared interferometry and  $i \approx 90^\circ$  from H<sub>2</sub>O maser observations showing evidence for a warped disk<sup>23</sup>. The hydrogen column density of the foreground absorption in the host galaxy is found to be  $N_{\text{H}}^{\text{host}} \approx 2 \times 10^{22} \text{ cm}^{-2}$ , which is consistent with the previous estimate from the optical extinction<sup>67</sup>, assuming that the absorber has similarly high metallicity as in the torus material and that dust mass is proportional to metal mass (that is, it has a 2.3 $\times$  larger dust-to-gas ratio than in the Galactic interstellar medium where hydrogen column density ( $N_{\text{H}}$ ) is related to optical Vband extinction ( $A_{\text{V}}$ ) as  $N_{\text{H}} \approx 2 \times 10^{21} \text{ cm}^{-2} A_{\text{V}}$ ). We have confirmed that our results on the metal abundances are little affected within the uncertainties in the fluxes of the contaminating sources. Because emission lines from the photoionized plasmas are spectroscopically separated from the neutral lines in the Resolve data, their effects on our elemental abundance measurements are ignorable.

We have determined the redshift parameters of the iron K $\alpha$  and K $\beta$  lines (with respect to the Hölzer et al.<sup>19</sup> values) to be  $z = 0.00155 \pm 0.00001 (\pm 0.00005)$  and  $z = 0.00158 \pm 0.00004 (\pm 0.00005)$ , respectively, after applying a heliocentric correction of 20 km s<sup>-1</sup> (that is, for the orbital motion of the Earth around the Sun; here, we have ignored the motion of the satellite relative to the Earth, which has a velocity amplitude of 8 km s<sup>-1</sup> with a period of 90 min and is averaged out during the observation). The errors in the parenthesis denote a gain calibration uncertainty of 0.3 eV (Resolve team, private communication). Thus, our results are consistent with the host galaxy redshift,  $z = 0.001448 \pm 0.000010$ , measured by H I observations<sup>73</sup>. For reference, Supplementary Table 1 summarizes the line centroid energies of major fluorescence lines in the literature based on ground experiments or theoretical calculations<sup>19,65,74,75</sup>. Note that the line energy depends on the chemical state of atoms by an order of 1 eV for iron K $\alpha$  (for example, ref. 76), which produces an additional systematic uncertainty in discussing the Doppler shift of the line emitter. Thus, a conservative limit on the line-of-sight velocity of the torus relative to the galaxy based on iron K $\alpha$  is  $-16$  to  $+78$  km s<sup>-1</sup> (the plus sign corresponds to a receding motion from us).

### Possible contamination in neutral line flux from diffuse emission

In our best-fit model, the spectrum of the CGX1 + diffuse component is modelled by a power law with a high energy cutoff and, hence, does not include any emission lines. However, if the diffuse emission around the nucleus contained a scattered component of the AGN emission off

cold gas, then it could contain fluorescence lines contaminating the line fluxes from the nucleus in the Resolve spectrum.

To evaluate its possible impact on the measurement of metal abundances of the torus, we estimate maximum fluxes of the fluorescence lines from the diffuse emission, using the continuum flux of the CGX1 + diffuse emission and theoretically expected equivalent widths in the scattered component from low column-density gas. Because the relative contribution from the diffuse emission becomes important at soft energies, here we focus on Ar K $\alpha$  and Ca K $\alpha$  lines. We have confirmed that the flux of diffuse emission in the 2.5–4.0 keV detected with Chandra is consistent with that inferred from our best-fit spectral model. Utilizing the Monte Carlo-based radiative transfer code SKIRT<sup>77</sup>, we calculate the X-ray reflection spectrum from neutral, constant density gas in a spherical geometry irradiated by the central source. We assume a power law spectrum with a photon index of 1.9 as the intrinsic emission, the chemical abundances in Extended Data Table 1 and a column density of  $10^{20} \text{ cm}^{-2}$  integrated from the centre to the outer radius of the sphere, which is necessary to account for the diffuse flux by Thomson scattering. This calculation yields the expected equivalent widths of 31 eV for Ar K $\alpha$  and 36 eV for Ca K $\alpha$ . By multiplying the continuum flux of the CGX1 + diffuse emission, we find that these correspond to fractions of 16% (Ar K $\alpha$ ) and 10% (Ca K $\alpha$ ) in the total line fluxes observed with Resolve, which are comparable to the  $1\sigma$  statistical uncertainties. These numbers should be taken as upper limits, because we assume that the CGX1 + diffuse components is fully attributed to a scattered component from cold gas, which is probably not the case; in fact, the Chandra spectrum of the diffuse emission within a radius of 6 arcsec around the nucleus shows no significant Ar K $\alpha$  line with a 90% upper limit on the equivalent width of 14 eV, a factor of 0.45 smaller than the above calculation. Thus, we conclude that our results on the metal abundances are robust. Note that the possible contamination from the diffuse emission, if any, works to strengthen our arguments on the subsolar abundance ratios of the Ar/Fe and Ca/Fe.

### Effects by adopting different torus geometry

To ensure that our results on the metal abundances do not depend on detailed spectral modelling of the torus reflection component, here we examine the effects by adopting different torus geometry. Here, we focus on (1) the size and number of clumps in the XCLUMPY model and (2) different spatial distribution of clumps from that in XCLUMPY.

**Size and number of clumps in XCLUMPY.** To examine the effect of adopting a different clump size from  $R_{\text{clump}} = 0.002$  pc (default value), we calculate the reflection spectra by adopting  $R_{\text{clump}} = 0.001$  pc or 0.005 pc by keeping the spectral parameters at the best-fit values in Extended Data Table 1. The results are plotted in Supplementary Fig. 7. As noticed, the spectra with different clump sizes in the 6.0–6.6-keV band are almost identical one another, including the line intensity and Compton shoulder fraction, which are important to constrain the iron to hydrogen abundance ratio ('Main'). Next, we change the number of clumps along the sight line on the equatorial plane,  $N_{\text{clump}}^{\text{equ}}$ , from 10 (default) to 5 or 15. We confirm that the resultant spectra in the 6.0–6.6-keV band again show no notable differences among them. Thus, we conclude that our results on the chemical abundances are robust against choices of  $R_{\text{clump}}$  and  $N_{\text{clump}}^{\text{equ}}$  in the XCLUMPY geometry.

**Clump distribution.** To examine if the torus reflection spectra sensitively depend on the clump configuration, here we consider a different torus geometry from that in XCLUMPY characterized by a circular-sector cross-section (Supplementary Fig. 3b). The geometry is similar to those adopted in the smooth torus models eTORUS<sup>60</sup> and BORUS<sup>62</sup>. The torus structure is defined by the following parameters: the torus angular width  $\theta$ , the number of clumps along the equatorial plane  $N_{\text{clump}}^{\text{equ}}$ , the equatorial column density  $N_{\text{H}}^{\text{equ}}$  and the inner and outer radii of the torus,  $r_{\text{in}}$  and  $r_{\text{out}}$ , respectively. Following the configuration

of the XCLUMPY model, we adopted  $r_{\text{in}} = 0.05$ ,  $r_{\text{out}} = 1$  and  $N_{\text{clump}}^{\text{Equ}} = 10$  for our simulations. The clumps are distributed uniformly and randomly.

The number density function,  $d(r, \phi, z)$  (in  $\text{pc}^{-3}$ ), is defined in a cylindrical coordinate system (where  $r$  is the radius,  $\phi$  is the azimuth and  $z$  is the height) as a constant value  $N$

$$d(r, \phi, z) = N, \quad (1)$$

where  $N$  is the normalization factor. This normalization is determined from the number of clumps along the equatorial plane,  $N_{\text{clump}}^{\text{Equ}}$ , via the relation

$$N_{\text{clump}}^{\text{Equ}} = \int_{r_{\text{in}}}^{r_{\text{out}}} d(r, 0, 0) \pi R_{\text{clump}}^2 dr, \quad (2)$$

$$N = \frac{N_{\text{clump}}^{\text{Equ}}}{\pi R_{\text{clump}}^2 (r_{\text{out}} - r_{\text{in}})}. \quad (3)$$

The total number of clumps in the torus,  $N_{\text{clump}}^{\text{Tot}}$ , is obtained by integrating the number density function over the torus volume

$$\begin{aligned} N_{\text{clump}}^{\text{Tot}} &= \int_{-(r_{\text{out}}-r_{\text{in}})\sin\theta}^{(r_{\text{out}}-r_{\text{in}})\sin\theta} \int_0^{2\pi} \int_{r_{\text{in}}+\sqrt{(r_{\text{out}}-r_{\text{in}})^2-z^2}}^{r_{\text{in}}+\sqrt{(r_{\text{out}}-r_{\text{in}})^2-z^2}} d(r, \phi, z) r dr d\phi dz \\ &= \frac{N_{\text{clump}}^{\text{Equ}} (r_{\text{out}} - r_{\text{in}}) (4(r_{\text{out}} - r_{\text{in}}) \sin\theta + 6r_{\text{in}}\theta)}{3R_{\text{clump}}^2}. \end{aligned} \quad (4)$$

We obtained a  $C$  statistic of 2,816.4 (Resolve, 2,316 bins) and  $\chi^2$  of 208.4 (FPMA, 232 bins) and 210.6 (FPMB, 212 bins), with 24 free parameters. This model yields the following parameters: a photon index of  $\Gamma = 1.92 \pm 0.05$ ,  $\theta = 13.5 \pm 0.7^\circ$ ,  $i = 78.2 \pm 0.7^\circ$  and an iron abundance of  $Z(\text{Fe}) = 2.21_{-0.04}^{+0.03}$  solar. Notably, the derived iron abundance is consistent with that obtained using the XCLUMPY model ( $Z(\text{Fe}) = 2.26 \pm 0.04$ ). This indicates that our results on the chemical abundances are not largely affected by the torus geometry adopted.

### Metal enrichment models

As described in ‘Main’, our benchmark model to interpret the observed abundance pattern consists of about 90% CCSNe with progenitors less massive than  $20 M_{\odot}$  and about 10% SNe Ia. We adopted the SN model by Nomoto et al.<sup>4</sup> for CCSNe and those by Fink et al.<sup>5</sup> and Shen et al.<sup>35</sup> for near- and sub- $M_{\text{Ch}}$  white dwarfs, respectively, assuming one-solar initial metallicity. We used the Salpeter IMF<sup>33</sup> to integrate the initial-mass-dependent CCSN yields, ignoring the contribution from HN. To ensure that our main results (that is, the high CCSN fraction and the presence of the upper mass limit for the progenitors of CCSNe) are robust against these assumptions, here we examine the effects by adopting other model settings.

**SN Ia models.** For the SN Ia model, we test two shock-propagation models in an exploding white dwarf: pure deflagration and delayed detonation. The three-dimensional hydrodynamical simulation utilized in Fink et al.<sup>5</sup> assumes the pure-deflagration scenario, whereas that in Seitenzahl et al.<sup>78</sup> adopts the delayed-detonation one. These two works also examine three initial core densities for yield calculation: normal, high and low. Accordingly, we try all six settings to fit our metal abundance pattern. For each setting, we adopt five different mass cutoffs for CCSNe progenitors. Supplementary Fig. 8 plots  $\chi^2/\text{degrees of freedom}$  values against the estimated SN Ia fractions. The upwards and downwards triangles represent the calculation with Seitenzahl et al.<sup>78</sup> and with Fink et al.<sup>5</sup>, respectively.

Most of them show a similar trend that the small upper mass limit provides a small fraction of SNe Ia and a better  $\chi^2$ . Lower SN Ia fractions than the representative case of Perseus (15–38%<sup>31</sup>, Supplementary Fig. 8,

grey shaded area) can only be achieved with the most severe upper limit of  $20 M_{\odot}$ . As for the densities of the ignition core, the normal density (approximately  $3 \times 10^9 \text{ g cm}^{-3}$ ) is preferred for pure deflagration, and the normal and high densities can be acceptable for delayed detonation. Despite the comprehensive analysis of galaxy clusters, it remains unclear which of pure deflagration or delayed detonation predominantly contributes to SN Ia enrichments in the universe. Hence, we do not conclude which SN Ia scenario is better based on our fitting results; instead, the difference between yields with pure deflagration and delayed detonation for a normal density dwarf is taken into account as uncertainty  $\sigma_{\text{Ia}}$  in the best-fitting model (Fig. 4).

**CCSN models. Alternative yield calculation.** Alternative CCSN calculations by Sukhbold et al.<sup>79</sup> are examined with both the pure-deflagration and delayed-detonation SNe Ia (Supplementary Fig. 8, pluses and crosses). We find that the classical calculations by Nomoto et al.<sup>4</sup> generally result in better fits and more reasonable fractions than Sukhbold et al.<sup>79</sup>. This trend is similar to that found by Mao et al.<sup>44</sup> for the starburst galaxy Arp 299. Thus, we adopt the yield of Nomoto et al.<sup>4</sup> as our benchmark for enrichment modelling.

**IMF.** We adopt the IMF-weighted yields of CCSNe using the top-heavy index of  $-1.0$ , considering the possibility that the IMF in starburst systems may follow a top-heavy behaviour rather than the Salpeter index of  $-2.3$  (for example, ref. 80). The results are given in Supplementary Fig. 8 with vertical rectangles. As noticed, the fraction of SNe Ia increases compared with the Salpeter case; this is naturally interpreted because massive progenitors make a greater contribution to metal enrichment with the top-heavy IMF than with the baseline case. By contrast, the bottom-heavy index of  $-3.0$  slightly reduces the SN Ia fractions as shown by horizontal rectangles in Supplementary Fig. 8, indicating that reducing the contribution from massive progenitors is essential to reproduce the observed abundance pattern. However, the bottom-heavy IMF model suppresses the SN Ia contribution less effectively than the assumption of the CCSN model with an upper mass limit.

**HN contribution.** We consider a possible contribution from the HN channel in massive stars<sup>4</sup>. To take HNe into account, we replace the CCSN yield tables for the massive progenitor regime ( $>20 M_{\odot}$ ) with the HN yields from Nomoto et al.<sup>4</sup>. The wherewithal to calculate the IMF-weighted yield follows the same strategy as described in the main text. The circles in Supplementary Fig. 8 represent the results of this CCSN + HN scenario. Although all cases show slightly lower SN Ia fractions with better  $\chi^2$  values than the pure CCSN case, the estimated values are still comparable to the Perseus environment; thus, this model would not be an alternative to the mass cutoff modelling.

**Progenitor metallicity.** Our measurement of the Fe/H ratio reveals supersolar metallicity (about 2 solar) in the Circinus centre. If this result is directly interpreted as metal-rich environments in starbursting regions, it motivates us to test high initial metallicity for CCSN progenitors. Since Nomoto et al.<sup>4</sup> extends their yield calculations to the supersolar metallicity regime, we adopt the CCSN yield tables of  $Z_{\text{CCSN}} = 0.05$  to replicate the benchmark modelling with white dwarf progenitors<sup>5,35</sup>. The resulting enrichment properties are summarized in Table 1 for the progenitor mass upper limits of  $40 M_{\odot}$ ,  $25 M_{\odot}$  and  $20 M_{\odot}$ . As noticed, the supersolar metallicity progenitors also prefer the mass cutoff CCSN model with a lower SN Ia fraction less than 10%, which is consistent with the benchmark scenario. Interestingly, the  $\chi^2$  values with  $Z_{\text{CCSN}} = 0.05$  are slightly better than with  $Z_{\text{CCSN}} = 0.02$ , implying that the bulk of CCSNe in the Circinus centre are from progenitors formed in a metal-rich environment. However, we keep our benchmark model at solar metallicity for a fair comparison and include the difference between the abundances with  $Z_{\text{CCSN}} = 0.02$  and  $Z_{\text{CCSN}} = 0.05$  as uncertainty  $\sigma_{\text{CC}}$  in the best-fitting model (Fig. 4).

### Mass transfer in circinus centre

Here, we show that the gas in the torus region must be transferred from outer regions on the basis of our metallicity measurement. Assuming the mass accretion rate of  $0.3 M_{\odot} \text{ yr}^{-1}$  at  $r = 0.27 \text{ pc}$  (ref. 22), the star formation rate of  $0.16 M_{\odot} \text{ yr}^{-1}$  within  $15 \text{ pc} \times 15 \text{ pc}$  (ref. 81), and the total gas mass of about  $10^6 M_{\odot}$  (ref. 16) within  $15 \text{ pc} \times 15 \text{ pc}$ , the depletion timescale (or replacement timescale assuming a steady state) is estimated to be  $2 \times 10^6 \text{ yr}$ . During this period, a total of  $3 \times 10^3$  SNe take place in the torus and produce an iron mass of  $200 M_{\odot}$ , corresponding to about 0.1 solar relative to the hydrogen mass. This is not sufficient to explain the observed metallicity in the Circinus centre (Fe/H of 2.3 solar), and therefore, metal-enriched gas must be transferred from the outer disk, for example, from  $r \approx 200 \text{ pc}$ , where a young starburst region was identified<sup>39</sup>.

### Data availability

The observational data analysed during this study are available via NASA's High Energy Astrophysics Science Archive Research Center (HEASARC) at <https://heasarc.gsfc.nasa.gov/> with observation IDs 000162000 (XRISM), 60901013002 (NuSTAR), 0932990101 (XMM-Newton) and 10223, 10224, 10225, 10226, 10832, 10833, 10842, 10843, 10844, 10850, 10872 and 10873 (Chandra). Line energies in the NIST atomic spectra database are available via NIST at <https://www.nist.gov/pml/atomic-spectra-database>.

### Code availability

The codes used for the data reduction are available via HEASARC at <https://heasarc.gsfc.nasa.gov/docs/software/heasoft> and via the ESA at <https://www.cosmos.esa.int/web/xmm-newton/sas>. The spectral fitting tools are available via NASA at <https://heasarc.gsfc.nasa.gov/xanadu/xspec> for XSPEC and via SRON at <https://zenodo.org/records/17313851> for SPEX.

### References

- Maiolino, R. & Mannucci, F. De re metallica: the cosmic chemical evolution of galaxies. *Astron. Astrophys. Rev.* **27**, 3 (2019).
- Hitomi Collaboration Solar abundance ratios of the iron-peak elements in the Perseus cluster. *Nature* **551**, 478–480 (2017).
- Lodders, K., Palme, H. & Gail, H.-P. in *Solar System, Landolt-Börnstein—Group VI Astronomy and Astrophysics* Vol. 4B (ed. Trümper, J.E.) 560–598 (Springer, 2009).
- Nomoto, K., Kobayashi, C. & Tominaga, N. Nucleosynthesis in stars and the chemical enrichment of galaxies. *Annu. Rev. Astron. Astrophys.* **51**, 457–509 (2013).
- Fink, M. et al. Three-dimensional pure deflagration models with nucleosynthesis and synthetic observables for type Ia supernovae. *Mon. Not. R. Astron. Soc.* **438**, 1762–1783 (2014).
- Nagao, T., Marconi, A. & Maiolino, R. The evolution of the broad-line region among SDSS quasars. *Astron. Astrophys.* **447**, 157–172 (2006).
- Nagao, T., Maiolino, R. & Marconi, A. Gas metallicity in the narrow-line regions of high-redshift active galactic nuclei. *Astron. Astrophys.* **447**, 863–876 (2006).
- Floris, A. et al. Chemical abundances along the quasar main sequence. *Astron. Astrophys.* **689**, 321 (2024).
- Tashiro, M. et al. X-ray imaging and spectroscopy mission. *Publ. Astron. Soc. Jpn.* **77**, 1–9 (2025).
- Freeman, K. C. et al. A large new galaxy in Circinus. *Astron. Astrophys.* **55**, 445–458 (1977).
- Oliva, E., Salvati, M., Moorwood, A. F. M. & Marconi, A. Size and physical conditions of the coronal line region in a nearby Seyfert 2: the Circinus galaxy. *Astron. Astrophys.* **288**, 457–465 (1994).
- Matt, G. et al. A reflection-dominated X-ray spectrum discovered by ASCA in the Circinus galaxy. *Mon. Not. R. Astron. Soc.* **281**, 69–73 (1996).
- Arévalo, P. et al. The 2–79 keV X-ray spectrum of the Circinus galaxy with NuSTAR, XMM-Newton, and Chandra: a fully Compton-thick active galactic nucleus. *Astrophys. J.* **791**, 81 (2014).
- Tanimoto, A. et al. XCLUMPY: X-ray spectral model from clumpy torus and its application to the Circinus galaxy. *Astrophys. J.* **877**, 95 (2019).
- Ramos Almeida, C. & Ricci, C. Nuclear obscuration in active galactic nuclei. *Nat. Astron.* **1**, 679–689 (2017).
- Wada, K., Schartmann, M. & Meijerink, R. Multi-phase nature of a radiation-driven fountain with nuclear starburst in a low-mass active galactic nucleus. *Astrophys. J.* **828**, 19 (2016).
- Shu, X. W., Yaqoob, T. & Wang, J. X. Chandra high-energy grating observations of the Fe K $\alpha$  line core in type II Seyfert galaxies: a comparison with type I nuclei. *Astrophys. J.* **738**, 147 (2011).
- Andonie, C. et al. A multiwavelength-motivated X-ray model for the Circinus galaxy. *Mon. Not. R. Astron. Soc.* **511**, 5768–5781 (2022).
- Hölzer, G., Fritsch, M., Deutsch, M., Härtwig, J. & Förster, E. K $\alpha_{1,2}$  and K $\beta_{1,3}$  X-ray emission lines of the 3d transition metals. *Phys. Rev. A* **56**, 4554–4568 (1997).
- Uematsu, R. et al. X-ray constraint on the location of the AGN torus in the Circinus galaxy. *Astrophys. J.* **913**, 17 (2021).
- Tristram, K. R. W. et al. ALMA imaging of the cold molecular and dusty disk in the type 2 active nucleus of the Circinus galaxy. *Astron. Astrophys.* **664**, 142 (2022).
- Izumi, T. et al. Supermassive black hole feeding and feedback observed on subparsec scales. *Science* **382**, 554–559 (2023).
- Greenhill, L. J. et al. A warped accretion disk and wide-angle outflow in the inner parsec of the Circinus galaxy. *Astrophys. J.* **590**, 162–173 (2003).
- Odaka, H., Yoneda, H., Takahashi, T. & Fabian, A. Sensitivity of the Fe K $\alpha$  Compton shoulder to the geometry and variability of the X-ray illumination of cosmic objects. *Mon. Not. R. Astron. Soc.* **462**, 2366–2381 (2016).
- Dimopoulos, G., Ricci, C. & Paltani, S. The Fe K $\alpha$  Compton shoulder in accreting supermassive black holes. *Mon. Not. R. Astron. Soc.* **532**, 4369–4388 (2024).
- Fischer, T. C., Crenshaw, D. M., Kraemer, S. B. & Schmitt, H. R. Determining inclinations of active galactic nuclei via their narrow-line region kinematics. I. Observational results. *Astrophys. J.* **209**, 1 (2013).
- Kakkad, D. et al. Dissecting the active galactic nucleus in Circinus—IV. MUSE-NFM observations unveil a tuning-fork ionized outflow morphology. *Mon. Not. R. Astron. Soc.* **519**, 5324–5332 (2023).
- Gandhi, P., Höning, S. F. & Kishimoto, M. The dust sublimation radius as an outer envelope to the bulk of the narrow Fe K $\alpha$  line emission in type 1 AGNs. *Astrophys. J.* **812**, 113 (2015).
- Xrism Collaboration XRISM spectroscopy of the Fe K $\alpha$  emission line in the Seyfert active galactic nucleus NGC 4151 reveals the disk, broad-line region, and torus. *Astrophys. J.* **973**, 25 (2024).
- Matt, G., Fabian, A. C. & Reynolds, C. S. Geometrical and chemical dependence of K-shell X-ray features. *Mon. Not. R. Astron. Soc.* **289**, 175–184 (1997).
- Simionescu, A. et al. Constraints on the chemical enrichment history of the Perseus cluster of galaxies from high-resolution X-ray spectroscopy. *Mon. Not. R. Astron. Soc.* **483**, 1701–1721 (2019).
- Nandakumar, G. et al. The first chemical census of the Milky Way's nuclear star cluster. *Astrophys. J.* **982**, 14 (2025).
- Salpeter, E. E. The luminosity function and stellar evolution. *Astrophys. J.* **121**, 161 (1955).
- Maiolino, R., Krabbe, A., Thatte, N. & Genzel, R. Seyfert activity and nuclear star formation in the Circinus galaxy. *Astrophys. J.* **493**, 650–665 (1998).

35. Shen, K. J., Kasen, D., Miles, B. J. & Townsley, D. M. Sub-Chandrasekhar-mass White Dwarf Detonations Revisited. *Astrophys. J.* **854**, 52 (2018).
36. Weinberg, D. H. et al. Chemical Cartography with APOGEE: Multi-element Abundance Ratios. *Astrophys. J.* **874**, 102 (2019).
37. Chen, X., Hu, L. & Wang, L. Constraining Type Ia Supernova Delay Time with Spatially Resolved Star Formation Histories. *Astrophys. J.* **922**, 15 (2021).
38. Zapartas, E. et al. Delay-time distribution of core-collapse supernovae with late events resulting from binary interaction. *Astron. Astrophys.* **601**, 29 (2017).
39. Marconi, A., Moorwood, A. F. M., Origlia, L. & Oliva, E. A prominent ionization cone and starburst ring in the nearby Circinus galaxy. *Messenger* **78**, 20–24 (1994).
40. Müller Sánchez, F. et al. SINFONI adaptive optics integral field spectroscopy of the Circinus Galaxy. *Astron. Astrophys.* **454**, 481–492 (2006).
41. Baker, W. M. et al. A core in a star-forming disc as evidence of inside-out growth in the early Universe. *Nat. Astron.* **9**, 141–154 (2025).
42. Wada, K. Radiation-driven fountain and origin of torus around active galactic nuclei. *Astrophys. J.* **758**, 66 (2012).
43. Villar Martín, M., López Cobá, C., Cazzoli, S., Pérez Montero, E. & Cabrera Lavers, A. AGN feedback can produce metal enrichment on galaxy scales. *Astron. Astrophys.* **690**, 397 (2024).
44. Mao, J. et al. Elemental abundances of the hot atmosphere of luminous infrared galaxy Arp 299. *Astrophys. J.* **918**, 17 (2021).
45. Heger, A., Fryer, C. L., Woosley, S. E., Langer, N. & Hartmann, D. H. How massive single stars end their life. *Astrophys. J.* **591**, 288–300 (2003).
46. Lovegrove, E. & Woosley, S. E. Very low energy supernovae from neutrino mass loss. *Astrophys. J.* **769**, 109 (2013).
47. Adams, S. M., Kochanek, C. S., Gerke, J. R. & Stanek, K. Z. The search for failed supernovae with the Large Binocular Telescope: constraints from 7 yr of data. *Mon. Not. R. Astron. Soc.* **469**, 1445–1455 (2017).
48. Smartt, S. J. Progenitors of core-collapse supernovae. *Annu. Rev. Astron. Astrophys.* **47**, 63–106 (2009).
49. Smartt, S. J. Observational constraints on the progenitors of core-collapse supernovae: the case for missing high-mass stars. *Publ. Astron. Soc. Aust.* **32**, 016 (2015).
50. Mochizuki, Y. et al. Optimization of x-ray event screening using ground and in-orbit data for the Resolve instrument onboard the XRISM satellite. In *Space Telescopes and Instrumentation 2024: Ultraviolet to Gamma Ray* Vol. 13093 (eds den Herder, J.-W.A., Nikzad, S. & Nakazawa, K.) 1309363 (Society of Photo-Optical Instrumentation Engineers Conference Series, 2024).
51. Porter, F. S. et al. In-flight performance of the XRISM/Resolve detector system. In *Space Telescopes and Instrumentation 2024: Ultraviolet to Gamma Ray* Vol. 13093 (eds den Herder, J.-W.A., Nikzad, S. & Nakazawa, K.) 130931 (Society of Photo-Optical Instrumentation Engineers Conference Series, 2024).
52. Eckart, M. E. et al. Energy gain scale calibration of the XRISM Resolve microcalorimeter spectrometer: ground calibration results and on-orbit comparison. In *Space Telescopes and Instrumentation 2024: Ultraviolet to Gamma Ray* Vol. 13093 (eds den Herder, J.-W.A., Nikzad, S. & Nakazawa, K.) 130931 (Society of Photo-Optical Instrumentation Engineers Conference Series, 2024).
53. Smith, D. A. & Wilson, A. S. A Chandra observation of the Circinus galaxy. *Astrophys. J.* **557**, 180–192 (2001).
54. Marinucci, A., Miniutti, G., Bianchi, S., Matt, G. & Risaliti, G. A Chandra view of the clumpy reflector at the heart of the Circinus galaxy. *Mon. Not. R. Astron. Soc.* **436**, 2500–2504 (2013).
55. Kawamuro, T., Izumi, T. & Imanishi, M. A Chandra and ALMA study of X-ray-irradiated gas in the central ~100 pc of the Circinus galaxy. *Publ. Astron. Soc. Jpn.* **71**, 68 (2019).
56. Fürst, F. Empirical correction of the EPIC effective area based on NuSTAR observations. *XMM-Newton Calibration Technical Note* <https://xmmweb.esac.esa.int/docs/documents/CAL-TN-0230-1-3.pdf> (2022).
57. Willingale, R., Starling, R. L. C., Beardmore, A. P., Tanvir, N. R. & O'Brien, P. T. Calibration of X-ray absorption in our Galaxy. *Mon. Not. R. Astron. Soc.* **431**, 394–404 (2013).
58. Wilms, J., Allen, A. & McCray, R. On the absorption of X-rays in the interstellar medium. *Astrophys. J.* **542**, 914–924 (2000).
59. Quirola-Vásquez, J. et al. The exceptional X-ray evolution of SN 1996cr in high resolution. *Mon. Not. R. Astron. Soc.* **490**, 4536–4564 (2019).
60. Ikeda, S., Awaki, H. & Terashima, Y. Study on X-ray spectra of obscured active galactic nuclei based on Monte Carlo simulation—an interpretation of observed wide-band spectra. *Astrophys. J.* **692**, 608–617 (2009).
61. Paltani, S. & Ricci, C. Reflex: X-ray absorption and reflection in active galactic nuclei for arbitrary geometries. *Astron. Astrophys.* **607**, 31 (2017).
62. Baloković, M. et al. New spectral model for constraining torus covering factors from broadband X-ray spectra of active galactic nuclei. *Astrophys. J.* **854**, 42 (2018).
63. Buchner, J., Brightman, M., Nandra, K., Nikutta, R. & Bauer, F. E. X-ray spectral and eclipsing model of the clumpy obscurer in active galactic nuclei. *Astron. Astrophys.* **629**, 16 (2019).
64. Nenkova, M., Sirocky, M. M., Nikutta, R., Ivezić, Ž & Elitzur, M. AGN dusty tori. II. Observational implications of clumpiness. *Astrophys. J.* **685**, 160–180 (2008).
65. Ito, Y. et al.  $K\alpha_{1,2}$  x-ray linewidths, asymmetry indices, and [K M] shake probabilities in elements Ca to Ge and comparison with theory for Ca, Ti, and Ge. *Phys. Rev. A* **94**, 042506 (2016).
66. Krause, M. O. & Oliver, J. H. Natural widths of atomic K and L levels, Ka X-ray lines and several KLL Auger lines. *J. Phys. Chem. Ref. Data* **8**, 329–338 (1979).
67. Roche, P. F. et al. Mid-infrared, spatially resolved spectroscopy of the nucleus of the Circinus galaxy. *Mon. Not. R. Astron. Soc.* **367**, 1689–1698 (2006).
68. Tristram, K. R. W. et al. Resolving the complex structure of the dust torus in the active nucleus of the Circinus galaxy. *Astron. Astrophys.* **474**, 837–850 (2007).
69. Mehdipour, M., Kaastra, J. S. & Kallman, T. Systematic comparison of photoionised plasma codes with application to spectroscopic studies of AGN in X-rays. *Astron. Astrophys.* **596**, 65 (2016).
70. McKaig, J. et al. Ray-tracing simulations of the soft X-ray scattered emission in obscured active galactic nuclei. *Mon. Not. R. Astron. Soc.* **526**, 5072–5083 (2023).
71. Tristram, K. R. W. et al. The dusty torus in the Circinus galaxy: a dense disk and the torus funnel. *Astron. Astrophys.* **563**, 82 (2014).
72. Isbell, J. W. et al. The dusty heart of Circinus. I. Imaging the circumnuclear dust in N-band. *Astron. Astrophys.* **663**, 35 (2022).
73. Koribalski, B. S. et al. The 1000 brightest hipass galaxies: H I properties. *Astron. J.* **128**, 16 (2004).
74. Ito, Y. et al. Structure of high-resolution  $K\beta_{1,3}$  x-ray emission spectra for the elements from Ca to Ge. *Phys. Rev. A* **97**, 052505 (2018).
75. Bearden, J. A. X-ray wavelengths. *Rev. Mod. Phys.* **39**, 78–124 (1967).
76. Bayda, E. & Öz, E. Chemical effects in the Ka and  $K\beta_{1,3}$  of X-ray emission spectra of Fe. *J. Electron. Spectrosc. Relat. Phenom.* **185**, 27–31 (2012).

77. Vander Meulen, B., Camps, P., Stalevski, M. & Baes, M. X-ray radiative transfer in full 3D with SKIRT. *Astron. Astrophys.* **674**, 123 (2023).
78. Seitzenthal, I. R. et al. Three-dimensional delayed-detonation models with nucleosynthesis for Type Ia supernovae. *Mon. Not. R. Astron. Soc.* **429**, 1156–1172 (2013).
79. Sukhbold, T., Ertl, T., Woosley, S. E., Brown, J. M. & Janka, H.-T. Core-collapse supernovae from 9 to 120 solar masses based on neutrino-powered explosions. *Astrophys. J.* **821**, 38 (2016).
80. Bastian, N., Covey, K. R. & Meyer, M. R. A universal stellar initial mass function? A critical look at variations. *Annu. Rev. Astron. Astrophys.* **48**, 339–389 (2010).
81. Davies, R. I. et al. A close look at star formation around active galactic nuclei. *Astrophys. J.* **671**, 1388–1412 (2007).
82. Kaastra, J. S. & Bleeker, J. A. M. Optimal binning of X-ray spectra and response matrix design. *Astron. Astrophys.* **587**, 151 (2016).

## Acknowledgements

We thank A. Miyamoto for her help in analysing the Chandra imaging data. This work was supported by JSPS KAKENHI (grant nos. JP22H00158, JP22H01268, JP22K03624, JP23H04899, JP21K13963, JP24K00638, JP24K17105, JP21K13958, JP21H01095, JP23K20850, JP24H00253, JP21K03615, JP24K00677, JP20K14491, JP23H00151, JP19K21884, JP20H01947, JP20KK0071, JP23K20239, JP24K00672, JP24K17104, JP24K17093, JP20K04009, JP21H04493, JP20H01946, JP23K13154, JP19K14762, JP20H05857, JP23K03459, JP24KK0070, JP24H01810, JP23K13153, JP24K00673, JP25H00672 and JP22KJ1990) and NASA (grant nos. 80NSSC23K0650, 80NSSC20K0733, 80NSSC18K0978, 80NSSC20K0883, 80NSSC20K0737, 80NSSC24K0678, 80NSSC18K1684 and 80NSSC22K1922). Y. Ueda acknowledges the support from the Kyoto University Foundation. E.B. was supported by the Israel Science Foundation (grant no. 2617/25). L.C. acknowledges support from NSF award 2205918. C.D. acknowledges support from STFC through grant no. ST/T000244/1. L. Gu acknowledges financial support from Canadian Space Agency grant no. 18XARMSTMA. A. Tanimoto and the present research are in part supported by the Kagoshima University postdoctoral research programme (KU-DREAM). Satoshi Yamada acknowledges support by the RIKEN SPDR Program. I.Z. acknowledges partial support from the Alfred P. Sloan Foundation through the Sloan Research Fellowship. M. Sawada acknowledges the support by the RIKEN Pioneering Project Evolution of Matter in the Universe (r-EMU) and Rikkyo University Special Fund for Research (Rikkyo SFR). N.W. and T.P. acknowledge the financial support of the GAČR EXPRO grant no. 21-13491X. Part of this work was performed under the auspices of the US Department of Energy by Lawrence Livermore National Laboratory under contract no. DE-AC52-07NA27344. The material is based upon work supported by NASA under award no. 80GSFC21M0002. This work was supported by the JSPS Core-to-Core Program (grant no. JPJSCCA20220002). The material is based on work supported by the Strategic Research Center of Saitama University. This work made use of the JAXA Supercomputer System Generation 3 (JSS3).

## Author contributions

As the leader of the Circinus galaxy target team in the XRISM Science Team (XST), Y. Ueda led this research project and wrote the manuscript. R.U. and S.O. led the data analysis, and K. Fukushima

led the interpretation of the results, all contributing to prepare the manuscript. M.G. and T. Yaqoob analysed the XRISM data, and A. Tanimoto reduced the NuSTAR data. K. Maeda, Y. Fujita, R.M., K. Matsushita, F.P., T.I., K. Fujiwara and Y.N. discussed the results. F.S.P., C.K. and M.E.E. contributed to the data calibration of Resolve and wrote the related section in the Methods. L. Gallo, E.K., Satoshi Yamada, J.M.M., T. Kawamuro, Y. Terashima, B.V.M., Y. Fukazawa, E.B. and L.C. provided comments on the content of the manuscript and helped to improve the manuscript. The science goals of XRISM were discussed and developed over 7 years by the XST, all members of which are authors of this manuscript. All the instruments were prepared by the joint efforts of the team. The Article was subject to an internal collaboration-wide review process. All authors reviewed and approved the final version of the manuscript.

## Competing interests

The authors declare no competing interests.

## Additional information

**Extended data** is available for this paper at <https://doi.org/10.1038/s41550-026-02817-6>.

**Supplementary information** The online version contains supplementary material available at <https://doi.org/10.1038/s41550-026-02817-6>.

**Correspondence and requests for materials** should be addressed to Yoshihiro Ueda, Ryosuke Uematsu, Shoji Ogawa or Kotaro Fukushima.

**Peer review information** *Nature Astronomy* thanks Johannes Buchner, Junjie Mao and the other, anonymous, reviewer(s) for their contribution to the peer review of this work.

**Reprints and permissions information** is available at [www.nature.com/reprints](http://www.nature.com/reprints).

**Publisher's note** Springer Nature remains neutral with regard to jurisdictional claims in published maps and institutional affiliations.

**Open Access** This article is licensed under a Creative Commons Attribution-NonCommercial-NoDerivatives 4.0 International License, which permits any non-commercial use, sharing, distribution and reproduction in any medium or format, as long as you give appropriate credit to the original author(s) and the source, provide a link to the Creative Commons licence, and indicate if you modified the licensed material. You do not have permission under this licence to share adapted material derived from this article or parts of it. The images or other third party material in this article are included in the article's Creative Commons licence, unless indicated otherwise in a credit line to the material. If material is not included in the article's Creative Commons licence and your intended use is not permitted by statutory regulation or exceeds the permitted use, you will need to obtain permission directly from the copyright holder. To view a copy of this licence, visit <http://creativecommons.org/licenses/by-nc-nd/4.0/>.

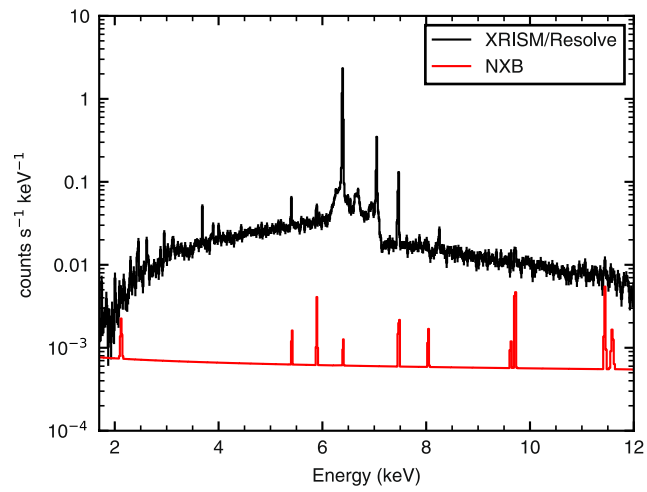
© The Author(s) 2026

## The XRISM Collaboration

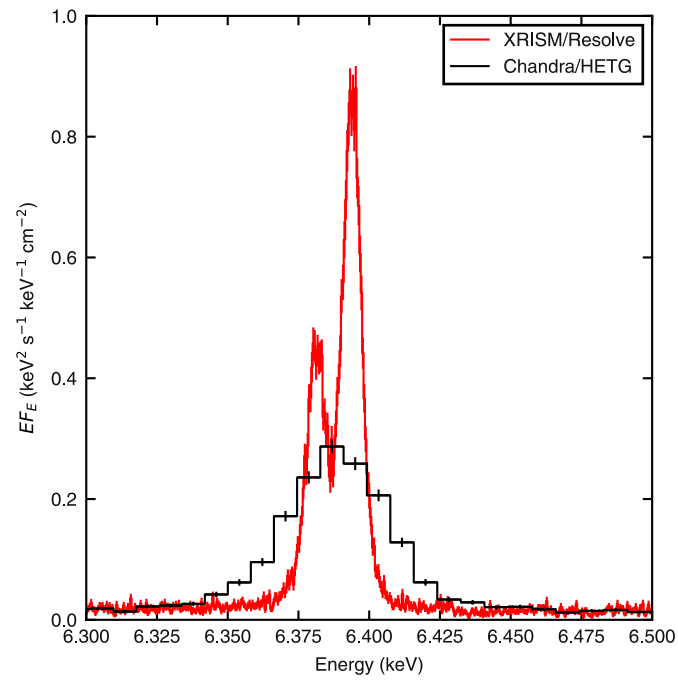
Marc Audard<sup>1</sup>, Hisamitsu Awaki<sup>2</sup>, Ralf Ballhausen<sup>3,4,5</sup>, Aya Bamba<sup>6</sup>, Ehud Behar<sup>7</sup>, Rozenn Boissay-Malaquin<sup>4,5,8</sup>, Laura Brenneman<sup>9</sup>, Gregory V. Brown<sup>10</sup>, Lia Corrales<sup>11</sup>, Elisa Costantini<sup>12</sup>, Renata Cumbee<sup>4</sup>, María Díaz Trigo<sup>13</sup>, Chris Done<sup>14</sup>, Tadayasu Dotani<sup>15</sup>, Ken Ebisawa<sup>15</sup>, Megan E. Eckart<sup>10</sup>, Dominique Eckert<sup>1</sup>, Teruaki Enoto<sup>16</sup>, Satoshi Eguchi<sup>17</sup>, Yuichiro Ezoe<sup>18</sup>, Adam Foster<sup>9</sup>, Ryuichi Fujimoto<sup>15</sup>, Yutaka Fujita<sup>18</sup>, Yasushi Fukazawa<sup>19</sup>,

Kotaro Fukushima<sup>15</sup>✉, Akihiro Furuzawa<sup>20</sup>, Luigi Gallo<sup>21</sup>, Javier A. Garcia<sup>4,22</sup>, Liyi Gu<sup>12</sup>, Matteo Guainazzi<sup>23</sup>, Kouichi Hagino<sup>6</sup>, Kenji Hamaguchi<sup>4,5,8</sup>, Isamu Hatsukade<sup>24</sup>, Katsuhiko Hayashi<sup>15</sup>, Takayuki Hayashi<sup>4,5,8</sup>, Natalie Hell<sup>10</sup>, Edmund Hodges-Kluck<sup>4</sup>, Ann Hornschemeier<sup>4</sup>, Yuto Ichinohe<sup>25</sup>, Daiki Ishi<sup>25</sup>, Manabu Ishida<sup>15</sup>, Kumi Ishikawa<sup>18</sup>, Yoshitaka Ishisaki<sup>18</sup>, Jelle Kaastra<sup>12,26</sup>, Timothy Kallman<sup>4</sup>, Erin Kara<sup>27</sup>, Satoru Katsuda<sup>28</sup>, Yoshiaki Kanemaru<sup>15</sup>, Richard Kelley<sup>4</sup>, Caroline Kilbourne<sup>4</sup>, Shunji Kitamoto<sup>29</sup>, Shogo Kobayashi<sup>30</sup>, Takayoshi Kohmura<sup>31</sup>, Aya Kubota<sup>32</sup>, Maurice Leutenegger<sup>4</sup>, Michael Loewenstein<sup>3,4,5</sup>, Yoshitomo Maeda<sup>15</sup>, Maxim Markevitch<sup>4</sup>, Hironori Matsumoto<sup>33</sup>, Kyoko Matsushita<sup>30</sup>, Dan McCammon<sup>34</sup>, Brian McNamara<sup>35</sup>, François Mernier<sup>3,4,5</sup>, Eric D. Miller<sup>27</sup>, Jon M. Miller<sup>11</sup>, Ikuyuki Mitsuishi<sup>36</sup>, Misaki Mizumoto<sup>37</sup>, Tsunefumi Mizuno<sup>38</sup>, Koji Mori<sup>24</sup>, Koji Mukai<sup>4,5,8</sup>, Hiroshi Murakami<sup>39</sup>, Richard Mushotzky<sup>3</sup>, Hiroshi Nakajima<sup>40</sup>, Kazuhiro Nakazawa<sup>36</sup>, Jan-Uwe Ness<sup>41</sup>, Kumiko Nobukawa<sup>42</sup>, Masayoshi Nobukawa<sup>43</sup>, Hirofumi Noda<sup>44</sup>, Hirokazu Odaka<sup>33</sup>, Shoji Ogawa<sup>15</sup>✉, Anna Ogorzalek<sup>3,4,5</sup>, Takashi Okajima<sup>4</sup>, Naomi Ota<sup>45</sup>, Stephane Paltani<sup>1</sup>, Robert Petre<sup>4</sup>, Paul Plucinsky<sup>9</sup>, Frederick Scott Porter<sup>4</sup>, Katja Pottschmidt<sup>4,5,8</sup>, Kosuke Sato<sup>28,46</sup>, Toshiki Sato<sup>47</sup>, Makoto Sawada<sup>29</sup>, Hiromi Seta<sup>18</sup>, Megumi Shidatsu<sup>2</sup>, Aurora Simionescu<sup>12</sup>, Randall Smith<sup>9</sup>, Hiromasa Suzuki<sup>15</sup>, Andrew Szymkowiak<sup>48</sup>, Hiromitsu Takahashi<sup>19</sup>, Mai Takeo<sup>28</sup>, Toru Tamagawa<sup>25</sup>, Keisuke Tamura<sup>4,5,8</sup>, Takaaki Tanaka<sup>49</sup>, Atsushi Tanimoto<sup>50</sup>, Makoto Tashiro<sup>15,28</sup>, Yukikatsu Terada<sup>15,28</sup>, Yuichi Terashima<sup>2</sup>, Yohko Tsuboi<sup>51</sup>, Masahiro Tsujimoto<sup>15</sup>, Hiroshi Tsunemi<sup>33</sup>, Takeshi G. Tsuru<sup>16</sup>, Ayşegül Tümer<sup>4,5,8</sup>, Hiroyuki Uchida<sup>16</sup>, Nagomi Uchida<sup>15</sup>, Yuusuke Uchida<sup>31</sup>, Hideki Uchiyama<sup>52</sup>, Yoshihiro Ueda<sup>53</sup>✉, Shinichiro Uno<sup>54</sup>, Jacco Vink<sup>55</sup>, Shin Watanabe<sup>15</sup>, Brian J. Williams<sup>4</sup>, Satoshi Yamada<sup>56</sup>, Shinya Yamada<sup>29</sup>, Hiroya Yamaguchi<sup>15</sup>, Kazutaka Yamaoka<sup>36</sup>, Noriko Yamasaki<sup>15</sup>, Makoto Yamauchi<sup>24</sup>, Shigeo Yamauchi<sup>45</sup>, Tahir Yaqoob<sup>4,5,8</sup>, Tomokage Yoneyama<sup>51</sup>, Tessei Yoshida<sup>15</sup>, Mihoko Yukita<sup>4,57</sup>, Irina Zhuravleva<sup>58</sup>, Kanta Fujiwara<sup>53</sup>, Takuma Izumi<sup>59,60,61,62</sup>, Taiki Kawamuro<sup>33</sup>, Keiichi Maeda<sup>53</sup>, Yuya Nakatani<sup>53</sup>, Frits Paerels<sup>63</sup>, Ryosuke Uematsu<sup>53</sup>✉ & Bert Vander Meulen<sup>23</sup>

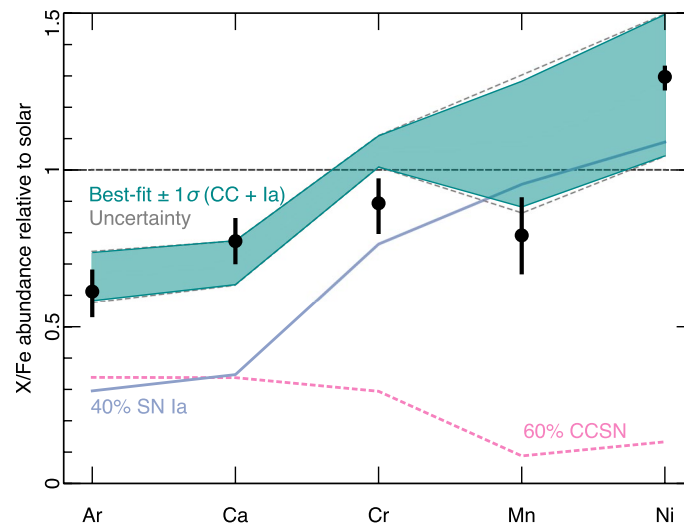
<sup>1</sup>Department of Astronomy, University of Geneva, Geneva, Switzerland. <sup>2</sup>Department of Physics, Ehime University, Ehime, Japan. <sup>3</sup>Department of Astronomy, University of Maryland, College Park, MD, USA. <sup>4</sup>NASA/Goddard Space Flight Center, Greenbelt, MD, USA. <sup>5</sup>Center for Research and Exploration in Space Science and Technology, NASA/GSFC (CREST II), Greenbelt, MD, USA. <sup>6</sup>Department of Physics, University of Tokyo, Tokyo, Japan. <sup>7</sup>Department of Physics, Technion, Technion City, Israel. <sup>8</sup>Center for Space Science and Technology, University of Maryland Baltimore County, Baltimore, MD, USA. <sup>9</sup>Center for Astrophysics, Harvard-Smithsonian, Cambridge, MA, USA. <sup>10</sup>Lawrence Livermore National Laboratory, Livermore, CA, USA. <sup>11</sup>Department of Astronomy, University of Michigan, Ann Arbor, MI, USA. <sup>12</sup>SRON Netherlands Institute for Space Research, Leiden, the Netherlands. <sup>13</sup>ESO, Garching, Germany. <sup>14</sup>Centre for Extragalactic Astronomy, Department of Physics, University of Durham, Durham, UK. <sup>15</sup>Institute of Space and Astronautical Science, Japan Aerospace Exploration Agency, Kanagawa, Japan. <sup>16</sup>Department of Physics, Kyoto University, Kyoto, Japan. <sup>17</sup>Department of Economics, Kumamoto Gakuen University, Kumamoto, Japan. <sup>18</sup>Department of Physics, Tokyo Metropolitan University, Tokyo, Japan. <sup>19</sup>Department of Physics, Hiroshima University, Hiroshima, Japan. <sup>20</sup>Department of Physics, Fujita Health University, Aichi, Japan. <sup>21</sup>Department of Astronomy and Physics, Saint Mary's University, Halifax, Nova Scotia, Canada. <sup>22</sup>Cahill Center for Astronomy and Astrophysics, California Institute of Technology, Pasadena, CA, USA. <sup>23</sup>European Space Agency, European Space Research and Technology Centre, Noordwijk, the Netherlands. <sup>24</sup>Faculty of Engineering, University of Miyazaki, Miyazaki, Japan. <sup>25</sup>RIKEN Nishina Center, Saitama, Japan. <sup>26</sup>Leiden Observatory, University of Leiden, Leiden, the Netherlands. <sup>27</sup>Kavli Institute for Astrophysics and Space Research, Massachusetts Institute of Technology, Cambridge, MA, USA. <sup>28</sup>Department of Physics, Saitama University, Saitama, Japan. <sup>29</sup>Department of Physics, Rikkyo University, Tokyo, Japan. <sup>30</sup>Faculty of Physics, Tokyo University of Science, Tokyo, Japan. <sup>31</sup>Faculty of Science and Technology, Tokyo University of Science, Chiba, Japan. <sup>32</sup>Department of Electronic Information Systems, Shibaura Institute of Technology, Saitama, Japan. <sup>33</sup>Department of Earth and Space Science, The University of Osaka, Osaka, Japan. <sup>34</sup>Department of Physics, University of Wisconsin, Madison, WI, USA. <sup>35</sup>Department of Physics and Astronomy, University of Waterloo, Waterloo, Ontario, Canada. <sup>36</sup>Department of Physics, Nagoya University, Aichi, Japan. <sup>37</sup>Science Research Education Unit, University of Teacher Education Fukuoka, Fukuoka, Japan. <sup>38</sup>Hiroshima Astrophysical Science Center, Hiroshima University, Hiroshima, Japan. <sup>39</sup>Department of Data Science, Tohoku Gakuin University, Miyagi, Japan. <sup>40</sup>College of Science and Engineering, Kanto Gakuin University, Kanagawa, Japan. <sup>41</sup>European Space Agency, European Space Astronomy Centre, Madrid, Spain. <sup>42</sup>Department of Science, Faculty of Science and Engineering, KINDAI University, Osaka, Japan. <sup>43</sup>Department of Teacher Training and School Education, Nara University of Education, Nara, Japan. <sup>44</sup>Astronomical Institute, Tohoku University, Miyagi, Japan. <sup>45</sup>Department of Physics, Nara Women's University, Nara, Japan. <sup>46</sup>Department of Astrophysics and Atmospheric Sciences, Kyoto Sangyo University, Kyoto, Japan. <sup>47</sup>School of Science and Technology, Meiji University, Kanagawa, Japan. <sup>48</sup>Yale Center for Astronomy and Astrophysics, Yale University, CT, USA. <sup>49</sup>Department of Physics, Konan University, Hyogo, Japan. <sup>50</sup>Graduate School of Science and Engineering, Kagoshima University, Kagoshima, Japan. <sup>51</sup>Department of Physics, Chuo University, Tokyo, Japan. <sup>52</sup>Faculty of Education, Shizuoka University, Shizuoka, Japan. <sup>53</sup>Department of Astronomy, Kyoto University, Kyoto, Japan. <sup>54</sup>Nihon Fukushi University, Shizuoka, Japan. <sup>55</sup>Anton Pannekoek Institute, the University of Amsterdam, Amsterdam, the Netherlands. <sup>56</sup>Frontier Research Institute for Interdisciplinary Sciences, Tohoku University, Sendai, Japan. <sup>57</sup>Johns Hopkins University, Baltimore, MD, USA. <sup>58</sup>Department of Astronomy and Astrophysics, University of Chicago, Chicago, IL, USA. <sup>59</sup>National Astronomical Observatory of Japan, Tokyo, Japan. <sup>60</sup>Department of Astronomy, The University of Tokyo, Tokyo, Japan. <sup>61</sup>Department of Astronomical Science, The Graduate University for Advanced Studies, SOKENDAI, Tokyo, Japan. <sup>62</sup>Amanogawa Galaxy Astronomy Research Center, Kagoshima University, Kagoshima, Japan. <sup>63</sup>Columbia Astrophysics Laboratory, Columbia University, New York, NY, USA. ✉e-mail: [fukushima.kotaro@jaxa.jp](mailto:fukushima.kotaro@jaxa.jp); [sogawa@ac.jaxa.jp](mailto:sogawa@ac.jaxa.jp); [ueda@kusastro.kyoto-u.ac.jp](mailto:ueda@kusastro.kyoto-u.ac.jp); [uematsu@kusastro.kyoto-u.ac.jp](mailto:uematsu@kusastro.kyoto-u.ac.jp)



**Extended Data Fig. 1 | Contribution of the non X-ray background (NXB) in the Circinus spectrum.** The red line denotes the modelled NXB spectrum. The black data points are the observed spectrum of Circinus (including the NXB) with error bars denoting the  $1\sigma$  confidence limits in photon statistics.



**Extended Data Fig. 2** | Comparison of the XRISM/Resolve spectrum and Chandra/HETG first order spectrum around the iron  $K\alpha$  line of Circinus. The former (this work) is binned with 0.5 eV. The latter is adopted from Uematsu et al.<sup>20</sup> and is binned with 9 eV. The error bars denote the  $1\sigma$  confidence limits in photon statistics.



**Extended Data Fig. 3 | Observed elemental abundances of the Circinus centre and theoretically calculated values with an upper mass limit of  $40 M_{\odot}$  for CCSN progenitors.** Relative abundances with respect to iron determined with XRISM ( $X/Fe$ , filled circles with error bars denoting  $1\sigma$  confidence limits estimated by Markov Chain Monte Carlo method) normalized to the corresponding proto-solar values (horizontal dashed line). The green shaded area represents the  $1\sigma$  uncertainty region of the best-fit model consisting of

( $60 \pm 10$ )% CCSNe from progenitor stars with  $< 40 M_{\odot}$ , ( $19 \pm 7$ )% near- $M_{\text{ch}}$  SNe Ia, and ( $21 \pm 11$ )% sub- $M_{\text{ch}}$  SNe Ia in number fraction, whose contributions to  $X/Fe$  are represented by the magenta, blue, and purple curves, respectively. Thin grey-dashed lines show the total uncertainty, including differences in the predicted yields by alternative SN Ia and CCSN modelling as  $\sqrt{\sigma_{\text{stat}}^2 + \sigma_{\text{Ia}}^2 + \sigma_{\text{CC}}^2}$  (see Methods Section 7).

Extended Data Table 1 | Best-Fit Parameters of XCLUMPY

Parameter	Value	Units
$Z^a$	$1.71 \pm 0.04$	solar
$Z(\text{Ar})^b$	$1.39^{+0.16}_{-0.20}$	solar
$Z(\text{Ca})^b$	$1.75 \pm 0.17$	solar
$Z(\text{Cr})^b$	$2.02^{+0.18}_{-0.22}$	solar
$Z(\text{Mn})^b$	$1.79 \pm 0.28$	solar
$Z(\text{Fe})^b$	$2.26 \pm 0.04$	solar
$Z(\text{Ni})^b$	$2.94^{+0.09}_{-0.11}$	solar
$N_{\text{H}}^{\text{equ}}$	$2.26^{+0.17}_{-0.16} \times 10^{25}$	$\text{cm}^{-2}$
$\sigma^c$	$9.2 \pm 0.3$	degree
$i$	$79.1 \pm 0.4$	degree
$\Gamma^d$	$1.90^{+0.05}_{-0.04}$	
$E_{\text{cut}}^e$	$65^{+7}_{-5}$	keV
$A^f$	$1.51^{+0.18}_{-0.16}$	photons $\text{cm}^{-1} \text{s}^{-1} \text{keV}^{-1}$
$L_{2-10}^g$	$8.84^{+0.63}_{-0.54} \times 10^{42}$	$\text{erg s}^{-1}$
$N_{\text{H}}^{\text{host } h}$	$1.66^{+0.16}_{-0.15} \times 10^{22}$	$\text{cm}^{-2}$
line width <sup>i</sup>	$210 \pm 10$	$\text{km s}^{-1}$

<sup>a</sup> Abundance of other metals than Ar, Ca, Cr, Mn, Fe, and Ni, relative to hydrogen.

<sup>b</sup> Abundance of the element in parenthesis relative to hydrogen.

<sup>c</sup> Torus angular width.

<sup>d</sup> Photon index of the intrinsic AGN component.

<sup>e</sup> Cutoff energy of the intrinsic AGN component.

<sup>f</sup> Normalization at 1 keV of the intrinsic AGN component.

<sup>g</sup> Intrinsic AGN luminosity in the 2–10 keV band (a distance of 4.2 Mpc is assumed).

<sup>h</sup> Hydrogen column density of the foreground absorption in the host galaxy.

<sup>i</sup> FWHM of the Gaussian kernel in velocity.

Errors denote the 1 $\sigma$  confidence limits.